

ALMA MATER STUDIORUM · UNIVERSITÀ DI  
BOLOGNA

---

Dipartimento di Fisica e Astronomia “Augusto Righi”  
Corso di Laurea in Fisica

## Facility for $\Lambda_c$ deuteron production in ALICE

Relatore:  
Prof. Andrea Alici

Presentata da:  
Giuseppe Luciano

Correlatore:  
Dott. Nicolò Jacazio

Anno Accademico 2024/2025



# Contents

<b>1 Abstract</b>	<b>5</b>
<b>2 Heavy-ion collision</b>	<b>7</b>
2.0.1 Concepts of quantum chromodynamics (QCD) . . . . .	7
2.0.2 The QCD phase diagram . . . . .	13
2.0.3 The different stage of a heavy-ion collision . . . . .	14
2.0.4 Centrality . . . . .	18
<b>3 Thermal model</b>	<b>21</b>
3.0.1 Hydrodynamical description . . . . .	21
3.0.2 Anisotropic flow . . . . .	27
3.0.3 Statistical Hadronisation Model (SHM) . . . . .	29
3.0.4 Strangeness and Charmness enhancement . . . . .	32
<b>4 <math>Y_cN</math> bound state</b>	<b>35</b>
4.0.1 One Boson exchange model . . . . .	35
4.0.2 $\Lambda_c$ N interaction . . . . .	37
4.0.3 Possible $\Lambda_c$ super-nuclei . . . . .	41
4.0.4 C-deuteron ( $c - d$ ) simulation . . . . .	43
<b>5 ALICE</b>	<b>49</b>
5.0.1 Inner Tracking System (ITS) . . . . .	52
5.0.2 Time projection chamber (TPC) . . . . .	53
5.0.3 Time Of Flight (TOF) . . . . .	55
5.0.4 Forward Detectors . . . . .	56
5.0.5 Track and vertex reconstruction . . . . .	58
<b>6 Appendix</b>	<b>63</b>
A Appendix A . . . . .	63
B Appendix B . . . . .	64
C Appendix C . . . . .	64

## Ringraziamenti

Un grazie speciale è dedicato a tutti i compagni di viaggio, sia a chi mi è stato vicino nelle interminabili ore sui treni che a quelli che mi hanno accompagnato durante il percorso accademico. I primi che con mirabile genitilezza si facevano annoiare dai miei racconti ma che erano sempre pronti a ricordarmi che esiste altro oltre a quello che posso vedere coi miei occhi. I secondi invece mi hanno insegnato ad approcciarmi ad una disciplina tanto affascinante quanto ostica fungendo da inesauribile fonte di ispirazione nel mostrarmi i possibili modi di interfacciarsi ai problemi, ognuno con la propria strategia. Sono stati compagni di interminabili e stravagnati conversazioni dal moto caotico ed imprevedibile, perchè spesso non lo si faceva per il risultato ma più per la genuina voglia di ragionare insieme. Sempre di fretta e sempre senza tempo eppure non si iniziava a lavorare seriamente senza prima aver proposto quell'improbabile argomento che ci bloccava per ore. Grazie ai miei grandi amici su cui ho sempre potuto contare anche se il tempo a loro dedicato non gli ha mai reso gustizia. A tutte quelle volte in cui non potevo uscire e a tutte le volte che mi hanno perdonato perchè se ti presenti con una bottiglia di cola sarebbe semplicemente folle continuare a tenere il broncio. Ma infine il pensiero principale è diretto ai miei genitori che anche se tornavo tardi avevano comunque la pazienza di aspettarmi per cena, che mi coccolavano nelle torride giornate di studio estivo con dell'acqua al limone ma nel bicchiere bello perchè anche l'occhio vuole la sua parte, che mi riportavano con i piedi per terra perchè a volte la fantasia ti stacca dal suolo, che a volte il vento non gonfia le vele ma la destinazione è lontana e bisogna remare, che a volte in certe serate persino la luna sembra più vicina ma non ci fai nemmeno caso, e che a volte serve una tesi per capire che non potrò mai ringraziarli abbastanza per tutti i sacrifici che hanno fatto per me.

# Chapter 1

## Abstract

Recent developments in hadron spectroscopy, particularly in the charm sector, have revealed that there may be different molecular bound states of hadrons, observed as hadron resonances. In particular, some studies suggest that the formation of molecules with particles containing a heavy quark is more plausible than we could have expected a few years ago. For this reason it was decided to explore the problem in more detail by focusing specifically on the c-deuteron, a super-nucleon consisting of a bound state between a  $\Lambda_c$  and a neutron. To do this, the Statistical Hadronisation Model was used to simulate the number of c-deuterons expected in a Pb-Pb collision as various parameters were varied. Dynamical simulations were then used to assess how the possible existence of this super-nucleus could increase the number of deuterons expected and the likelihood of their detection by the ALICE detector. I risultati ottenuti sono stati di



# Chapter 2

## Heavy-ion collision

### 2.0.1 Concepts of quantum chromodynamics (QCD)

Before talking about the dynamics of heavy-ion collision and c-deuteron production we should introduce some concepts coming from quantum chromodynamics (QCD) and the standard model (SM). The SM describes the universe at its most fundamental level and correctly predicts many results of the experiments we have ever done, sometimes with unprecedented accuracy. This theory can explain the interaction of particles with three different forces: the strong nuclear force, the weak nuclear force, and electromagnetism; while the gravity force is not yet part of the Standard Model [36]. Fortunately the absence of a quantum gravity theory, that is maybe the most fundamental lack of the SM, is not too influent in the experiment that we can actually perform. In fact physicist believe that the gravity influence will became evident only at the plank scale. This region may be characterized by particle energies of around  $10^{19}$  GeV or  $10^9$  J on a single particle. The same kinetic energy of a Jumbo jet that travel at  $\approx 250$  km/h. However the SM is very extended in this thesis we will only focus on the essential aspect for understanding the following chapter.

The QCD, a theory included in the SM, is the most successful theory to explain the strong interaction. The QCD assumed that strong nuclear force act on the quarks and is mediated by gluons. The quark are elementary particle introduced by Gell-Mann and Zweig for understand the "proliferation of the hadron". In fact, historically, when the energy of the collision start to increase different particle that interact with the strong force, called hadrons, were discovered. So, for explain the hundred of different hadrons detect, the two scientist proposed that this structures come form different combination of more fundamental particle, the quark. In particular the name quark come from the Finnegan's wake, a book of James Joyce, a writer that Gell-Mann loved. Nowadays we know six different type (flavor) of quark usually divided in three generation. The first generation include quark up (u) and down (d), the second the quark strange (s) and charm (c), and the last one the quark

top (t) and bottom (b).

Instead the quantum chromodynamics takes it's name because it introduces a property called color charge, the QCD analog of electric charge. First hint about the real existence of color charge was given with the discovery of  $\Delta^{++}$  baryon in 1951. This baryon could only be explained imaging that it is composed of three quark up with the spin aligned. So the configuration of the particle could be written as follows

$$|\Delta^{++}\rangle = |u_\uparrow u_\uparrow u_\uparrow\rangle$$

A highly symmetric configuration. However, since the particles that compose it are fermions, for the Pauli principle, they must have an overall antisymmetric wave function. In 1965, fourteen years after its discovery, this problem was finally understood by the introduction of the charge of colour. With this new parameter we can add another inner space associated to the particle and is configuration can be written as.

$$|\Delta^{++}\rangle = |u_\uparrow u_\uparrow u_\uparrow\rangle \epsilon_{ijk} [C_i \otimes C_j \otimes C_k]$$

where  $\epsilon_{ijk}$  is the Ricci's tensor that permit the wave function to be anti-symmetric under quark exchange. This is only an example but other strong support of the color charge assumption had been discovered with the passing of time.

Quantum Chromodynamics is based on the gauge group SU(3), the Special Unitary group in 3 (complex) dimensions, whose elements are the set of unitary  $3 \times 3$  matrices with determinant one. Since there are 9 linearly independent unitary complex matrices in three dimension, the condition on the determinant reduced the set at 8 independent directions in this matrix space, corresponding to eight different generators of the group. On a physical level the presence of eight generator predict the existence of eight different gluons. The Lagrangian density of QCD is

$$\mathcal{L} = i\bar{\psi}_q^i \gamma^\mu (D_\mu)_{ij} \psi_q^j - m_q \bar{\psi}_q^i \psi_{iq} - \frac{1}{4} F_{\mu\nu}^a F^{a\mu\nu}$$

(2.1)

where  $\psi_q^i$  denotes a quark field with colour index,  $\gamma^\mu$  is a Dirac matrix that expresses the vector nature of the strong interaction, with  $\mu$  being a Lorentz vector index,  $m_q$ , the mass of the quark, allows for the possibility of non-zero quark masses,  $F_{\mu\nu}^a$  is the gluon field strength tensor for a gluon and  $D_\mu$  is the covariant derivative in QCD given by  $(D_\mu)_{ij} = \delta_{ij} \partial_\mu - ig_s t_{ij}^a A_\mu^a$ , with  $g_s$  the strong coupling constant [41]. The coupling constant is maybe the most important parameter in defying the properties of the theory, we can imaging it as the probability that a partons, therm used for indicate both gluon and quark, of interact in each instant of time whit other partons. The possible vertices of interaction between partons are visible in Fig 2.2. Since this value is considerable during a process the higher order Feynman diagram cannot be

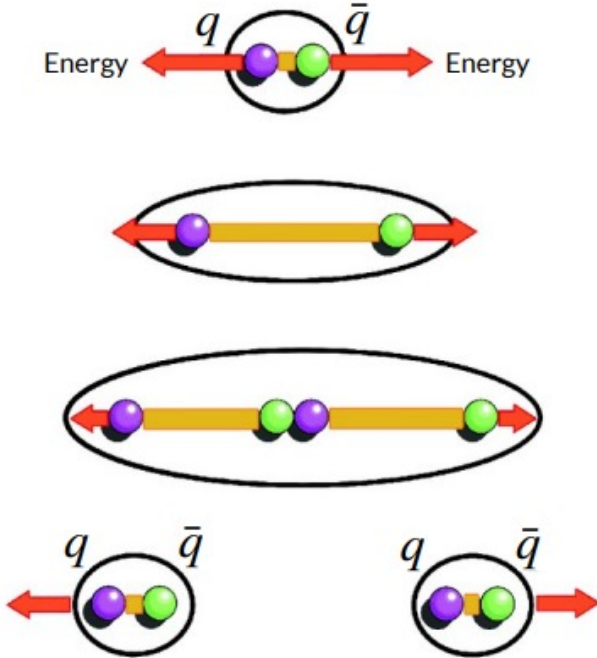


Figure 2.1: The figure resume the process of pair production of quark. [32]

neglected therefore is particularly difficult to perform analytical calculus. So, as it is said in this cases, the theory is not perturbatively tractable. The QCD exhibit three salient properties: color confinement, asymptotic freedom and the chiral symmetry breaking.

Starting from the first one we can say that unlike one may think watching at Eq 2.1 since the gluon are massless the QCD should be a long range force. Instead the common experience tell us that only at very close distances the effect of the interaction are visible. This is possible because the energy for separate the quark grows until a quark–antiquark pair is spontaneously produced, turning the initial hadron into a pair of hadrons instead of isolating a color charge, a graphical resume is visible in Fig 2.1. This is a very efficient way for dissipate the energy and the final result is the production of jets of hadron clearly visible in the experimental data. For these reasons, physicists believe that a direct consequence of the theory is "colour confinement", which rules out the possibility of finding a free quark. However, a formal proof has not yet been obtained and this problem has been added to the list of Millennium Prize Problems.

The asymptotic freedom is a reduction in the strength of interactions between quarks and gluons as the energy scale of those interactions increases. In fact, if the transferred momenta during a collision is low we cannot penetrate the cloud of virtual process associated to a particle. Instead, if the transferred momenta increase we can penetrate deeper in the virtual process cloud and so analyze in more detail the "naked particle". The possibility of

penetrate deeper in the cloud of virtual process associated to a particle allow us to observe different behaviors of this latter. The asymptotic freedom is related to the fact that the quark-antiquark loop has a shielding effect of the color charge and the gluon loop has an anti screening effect. In particular hold that for the coupling constant that.

$$g_s(Q^2) = \frac{g_s(\mu^2)}{1 + g_s(\mu^2) \frac{11n_c - 2n_f}{12\pi} \ln\left(\frac{Q^2}{\mu^2}\right)} = \frac{g_s(\mu^2)}{1 + g_s(\mu^2) \frac{21}{12\pi} \ln\left(\frac{Q^2}{\mu^2}\right)} \quad (2.2)$$

where  $\mu$  is a generic transferred quadri-momenta as  $Q$ ,  $n_f$  is the number of known flavor (assumed six in the SM),  $n_c$  the number of color (assumed three). Is possible to observe that  $11n_c > 2n_f$  and for these reason the anti-shielding effect of the gluon loop is prevalent. From the Eq 2.2 we can desume that the coupling decrease when the transferred momenta increase. the Eq 2.2 is usually expressed showing the scale factor.

$$g_s(Q^2) = \frac{1}{\frac{1}{g_s(\mu^2)} + \frac{21}{12\pi} \ln\left(\frac{Q^2}{\mu^2}\right)} \quad (2.3)$$

defining

$$\frac{1}{g_s(\mu^2)} = \frac{21}{12\pi} \ln\left(\frac{\mu^2}{\Lambda_{CQD}^2}\right) \quad (2.4)$$

$$g_s(Q^2) = \frac{1}{\frac{21}{12\pi} \ln\left(\frac{\mu^2}{\Lambda_{CQD}^2}\right) + \frac{21}{12\pi} \ln\left(\frac{Q^2}{\mu^2}\right)} = \frac{1}{\frac{21}{12\pi} \ln\left(\frac{Q^2}{\Lambda_{CQD}^2}\right)} \quad (2.5)$$

In this way is more evident the point that made the logarithm diverge and the QCD became perturbatively tractable. Experimentally it is found  $\Lambda \sim 200 \div 300$  Mev [13]. The asymptotic freedom of QCD was discovered in 1973 by David Gross and Frank Wilczek, [16]. and independently by David Politzer in the same year. For this work, all three shared the 2004 Nobel Prize in Physics. With the advent of computers, it has become possible to perform lattice QCD simulations. These simulations can be carried out in the non-perturbative condition to study the strong interaction by discretizing spacetime into a lattice, which makes it possible to calculate the behavior of quarks and gluons numerically. Before the advent of these advanced computing resources, such detailed simulations were impractical due to the immense complexity of solving the QCD equations at low energies. However, lattice QCD simulations can be very expensive and compromises became essential.

In conclusion we can talk about the Chiral symmetry breaking. Massless fermions in Dirac theory are described by left or right-handed spinors. The difference is related to the fact that a particle can have spin either aligned (right-handed chirality), or counter-aligned (left-handed chirality), with his momenta. In the case of massless fermion chirality is a conserved quantum number and the left and right handed spinors can be independently phase

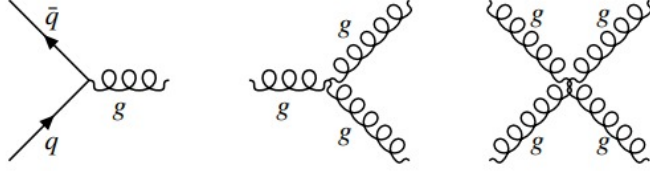


Figure 2.2: The figure show the basilar Feynman diagram of QCD.

transformed. A Dirac mass term explicitly breaks the symmetry but in QCD, the lowest mass quarks are nearly massless and exist an approximate chiral symmetry making the system spontaneously prefer a certain configuration. In fact the vacuum in QCD is non-trivial. It is not simply empty space, but has a rich structure in which quark-antiquark pairs are constantly created and annihilated. For this reason, it is described as a superposition of many states, and the interactions between quarks and gluons cause the system to favour a particular configuration, which spontaneously breaks the chiral symmetry. The spontaneous symmetry breaking produces hadrons masses far above the one of the quarks. Yoichiro Nambu was awarded the 2008 Nobel Prize in Physics for elucidating the phenomenon in 1960. Lattice simulations have confirmed all his generic predictions. [35]

For our discussion the Polyakov loop operator gets a particular importance.

$$L = \frac{1}{3} Tr \left( P e^{ig \int_0^\beta d\tau A_4(\vec{x}, \tau)} \right) \quad (2.6)$$

Where  $P$  is the path-ordering operator and  $A_4$  is the Euclidean temporal component of the gauge field and  $\beta = \frac{1}{T}$  in natural unit,  $T$  temperature. A vanishing thermal expectation value  $\langle L \rangle$  of the Polyakov loop operator thus indicates infinite energy for a free quark, i.e. quark confinement. It's possible to proof that as the temperature increases  $\langle L \rangle$  increases rapidly to a nonzero value at high temperatures. This indicates that quark confinement is broken at the corresponding critical temperature  $T_{cr}$ . Experimentally it is found that  $T_{cr} \sim 160$  MeV, which corresponds approximately to  $1.86 \cdot 10^{12}$  K [21]. However, this doesn't mean that we can find free quark, because the strong force is still there and the quark can't escape by flying away.

We have already discuss that in the absence of quark masses the Eq 2.1 is chirally symmetric. Since the up and down quark masses are very small, neglecting them is a good approximation. Anyway when the temperature decrease the approximate chiral symmetry breaks generating a dynamic mass, the so called "constituent" masses. In vacuum this constituent mass are thus about 300 MeV for the up and down quarks, about 450 MeV for the strange quark, 1.5 Gev for the charm, 4.5 Gev for bottom and 180 Gev for top [13]. The dynamically generated mass disappeared at  $T_{cr}$ , making the quarks light again and restoring the approximate chiral symmetry of QCD. The dissolution of massive hadrons into almost massless quarks and gluons at  $T_{cr}$  leads to

a very rapid rise of the energy density near the deconfinement transition, as shown in Fig 2.3. For a massless gas of quarks and gluons the energy density is

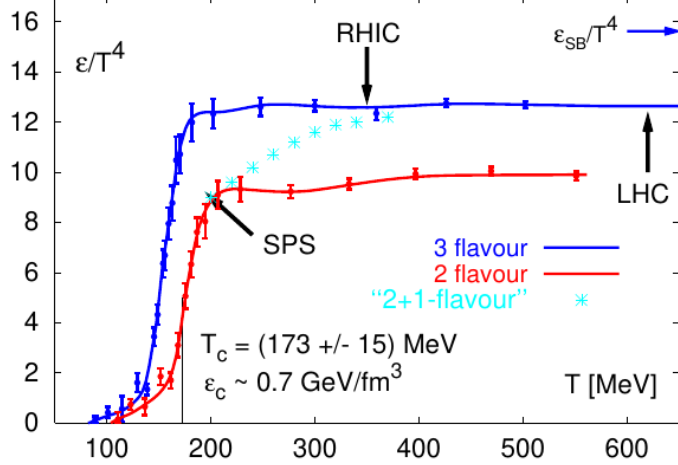


Figure 2.3: The symbol  $\epsilon$  stands for energy density, the curves labelled “2 flavour” and “3 flavor” were calculated for two and three light quark flavors, “2+1 flavour” indicates a calculation for two light and one heavier strange quark flavor.

proportional to  $T^4$ . We see that for  $T < 4T_{cr}$  the data remain about 20% below this Stefan-Boltzmann limit. Instead near  $T_{cr}$  the ratio  $\epsilon/T^4$  drops rapidly by more than a factor 10. This is due to hadronization that we will discuss in the following chapter. The much heavier hadrons are exponentially suppressed below  $T_{cr}$ , leading to a much smaller number of equivalent massless degrees of freedom. According to Fig 2.3 the critical energy density for deconfinement is about  $0.6 \div 0.7$  GeV/ $fm^3$ . However we can have information about the temperature and not directly on the energy density. So the uncertainty of  $\pm 15$  Mev reported in the graph on  $T_{cr}$  introduce a  $\pm 40\%$  uncertainty in the critical energy density, thanks to the  $T^4$  proportional relation, which could be as large as  $1$  GeV/ $fm^3$  or as small as  $500$  MeV/ $fm^3$ . The dependence of  $T^4$  is particularly important because for exceed the critical temperature by only 30% in order to reach the upper edge of the transition region, an energy density  $\epsilon \approx 3.5$  GeV/ $fm^3$  is required and to reach  $2T_{cr}$  the energy density needed arrived at  $23$  GeV/ $fm^3$  [20]. The former number is approximately the value obtained in Pb-Pb collisions at  $\sqrt{s_{NN}} = 17$  GeV. Under the assumption that the total momentum in the region is null we can compute the energy density for colliding nuclei as

$$\langle \epsilon \rangle = 2\rho_0 \gamma^2 = \frac{\sqrt{s_{NN}}^2}{2Vm c^2} \quad (2.7)$$

where  $\rho_0$  indicates the energy density at rest of each nucleus and  $\gamma$  is the Lorentz factor of the beam,  $V$  the volume and  $m$  the mass. In heavy ion

collision at the Relativistic Heavy Ion Collider (RHIC) for Au-Au collision at  $\sqrt{s_{NN}} = 200$  GeV and  $R \approx 6.98$  fm  $\langle \epsilon \rangle = 3 \cdot 10^3$  GeV/fm $^3$  while for Pb-Pb collision at  $\sqrt{s_{NN}} = 5.02$  TeV and  $R \approx 7.11$  fm  $\langle \epsilon \rangle = 2 \cdot 10^6$  GeV/fm $^3$ , much larger than  $\epsilon_{cr}$ . A more precise formulation of the energy density, valid as long as the particle production exhibits a “plateau” structure in the central rapidity region and the net baryon number at mid-rapidity is close to zero, was given by Bjorken [11]

$$\langle \epsilon_B \rangle = \frac{1}{\tau_f \pi R^2} \frac{d\langle E \rangle}{dy} \quad (2.8)$$

Where  $\tau_f$  stands for the formation time of the fireball and  $R$  is the transverse radius of the participant volume for these reason and  $\pi R^2$  is the nuclei overlap area and  $y$  is the rapidity  $y = \frac{1}{2} \ln \frac{E+p_z c}{E-p_z c}$  where  $z$  is the axis in witch the beam is aligned. [22]

### 2.0.2 The QCD phase diagram

Under extreme conditions of density and temperature, hadrons “melt” and release their contents of quarks and gluons. This is possible because at short distances and large momentum transfers, the strong interaction is not intense enough to bring the partons together and hadron structures are no longer possible. Color charges are then deconfined, and this state is called Quark-Gluon Plasma (QGP). For these reason is possible to consider QGP as the deconfined state of QCD matter and is hottest and most dense liquid known to humankind and, according to the most widely accepted cosmological model, the  $\Lambda$ CDM, were the condition of our universe only few microseconds after the Big Bang[18].

The ordinary nuclear matter is located at approximately  $T \approx 0$  MeV and  $\mu_B \approx m_N \approx 0.94$  GeV (neutron mass).The baryon chemical potential  $\mu_B$  is a thermodynamic coordinate like temperature, best understood as the energy required by the system to change its chemical composition. It is tightly connected with the density of quarks: when the former is zero, the latter vanished as well, but we will discuss it better later. A simple description of the phases of nuclear matter is given in Fig. 2.4. Particularly problematic is the study of the diagram when  $\mu_B$  approaches zero, like in the condition of the primordial universe. As illustrate in Fig 2.4 lattice QCD provides evidence that, even for realistically small up and down quark masses, the transition at  $\mu_B = 0$  is a first order rapid crossover; although the precise value where the transition occur still remains to be determined. The short line visible in correspondence  $\mu_B = 1$  GeV indicates the nuclear liquid-gas phase transition, with a critical endpoint at a temperature of about 7.5 MeV. At higher temperatures more and more hadron resonances are excited and we have a hadron resonance gas.

At low temperatures and asymptotically large baryon densities quarks are also deconfined, although not in a quark-gluon plasma state but rather in

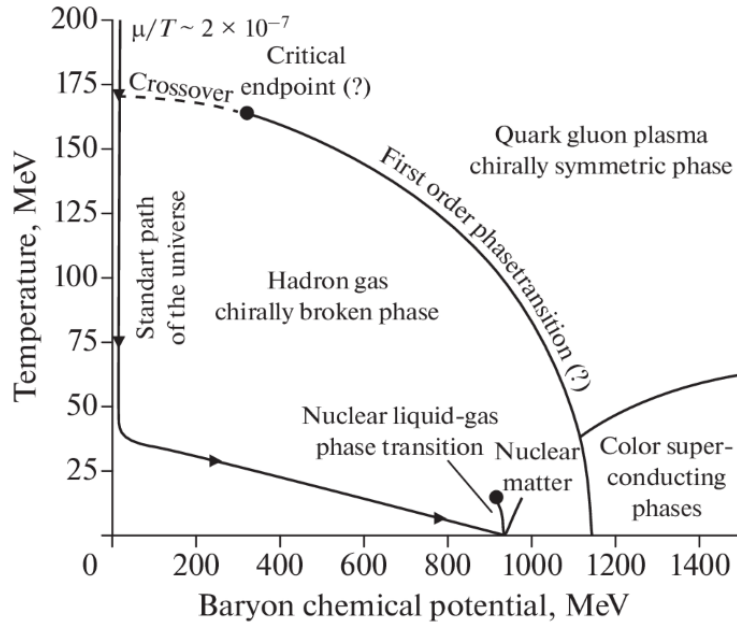


Figure 2.4: A sketched view of the phase diagram of strongly interacting matter, in the plane of temperature and the baryon chemical potential that represents the amount of net baryon charge available in the system [40]

a color superconductor state. In these condition matter carries color charge without loss, analogous to the conventional superconductors that can carry electric charge without loss. The superconducting state is separated from the QGP by a first order transition at a critical temperature estimated to be of order 30-50 MeV. It is important to note that heavy-ion collisions are not a viable method for probing the colour-superconducting phase. This is due to the fact that the process of compressing nuclear matter in such collisions results in significant entropy production and consequent heating.

As the centre-of-mass collision energy increases, the colliding nuclei become increasingly transparent with respect to each other. Consequently a decreasing fraction of the beam energy and of the incoming baryons get stopped in the center of mass. When the energy increase the incoming net baryons becoming more baryon-antibaryon symmetric bringing  $\mu_B$  closer to zero. At the LHC the entropy per baryon ratio S/A can reach several thousand, still far from the early universe ratio of  $10^9$ , that is, for all practical purposes, “baryon-free” ( $\mu_B = 0$ ) QCD matter. [20].

### 2.0.3 The different stage of a heavy-ion collision

The main stages of relativistic heavy-ion collisions are: Pre-equilibrium, thermalization, hadronization, Chemical freeze-out, and decoupling. This section came from the following article [20], [21], [34], [8] and [22].

1. **Collision:** At  $t=0$  the collision take place. The nuclei are highly Lorentz contracted and an extremely dense region of partons is generated with a large energy deposit in the overlap region of the collision. The superposition occur in in  $t_{coll} = 2 \frac{R_N}{\gamma}$ , where  $R_N$  is the nucleus radius. In Pb-Pb collision at  $\sqrt{s_{NN}} = 5.02$  TeV  $t_{coll} \sim 6 \cdot 10^{-3}$  fm/c, smaller than the strong-interaction timescale  $t_{QCD} \sim 1$  fm/c.
2. **Pre-equilibrium** ( $t < 1$  fm/c): The two nuclei just collided. The partons of the participating nucleon interact producing a large amount of quarks and gluons. This process leads to generate high-momentum partons (the transverse momenta is  $p_\perp \gg 1$  GeV/c) creating jets or heavy quark with the emission of prompt photons. The system is now formed by a dense inhomogeneous droplet of strongly interacting QGP matter. In the very early collision stages the momentum transferred is huge and the particle production can be calculated in perturbative QCD. According to the Heisemberg uncertainty relation the production happens on a time scale  $t \sim \frac{1}{\sqrt[2]{Q^2}}$ , where  $Q$  is the momentum transfers. The key difference between elementary particle and nucleus-nucleus collisions is that the quanta created in the primary collisions between the incoming nucleons can't right away escape into the surrounding vacuum.

In a central collision between two Pb or Au nuclei the nuclear reaction zone has a transverse diameter of about 12 fm, so a hard particle created near the edge and moving towards the center (straight inward) needs about 20 fm/c before it emerges on the other side. During this time the matter thermalizes, expands, cools down and almost reaches decoupling. As the particle moves through the plasma, it loses energy. It can be shown that the energy loss is proportional to the density of the medium times the scattering cross section between the probe and the medium constituents integrated along the trajectory of the probe. In this way, important information about the medium can be analysed. Other probes of the early collision stage are direct photons, either real or virtual, and other process connected to QED such the creation of a couple lepton-antilepton generally known as “dileptons”. In contrast to all hadronic probes, they thus escape from the collision zone without reinteraction and carry pristine information about the momentum distributions of the particle that generated them. Anyway the directly emitted photons and dileptons must be must be searched in a chaotic background of indirect photons and particle generated in other process, This renders the measurement of these signals difficult.

3. **Thermalization** ( $t \sim 1 - 15$  fm/c): The constituents of the fireball frequently interact, establishing a local equilibrium state. The time taken to establish a local thermodynamic equilibrium is called the thermalization time. This phase is characterized by a thermally equilibrated

nature that make the QCP exhibit a perfect fluid behavior and allowing a hydrodynamic descriptions of the medium. This refers to its exceptionally low viscosity, minimal internal friction and high thermal conductivity. Experimental observations, particularly those related to the collective flow of particles produced in heavy-ion collisions, support this behaviour. The produced partons rescatter both elastically and inelastically. Both types of collisions lead to equipartitioning of the deposited energy, but only the inelastic ones change the chemical composition of the medium by changing the flavor of partons. The system, now in equilibrium, builds an internal pressure that finds no opposition by the void that surrounds it. This leads to a rapid hydrodynamic expansion of the system with a decrease in temperature and energy density.

4. **Hadronization** ( $t \sim 20$  fm/c) As the temperature lowers, the system energy density is not able to keep partons separated and hadrons start to form when the energy density approach  $\epsilon_{cr}$ . During this phase transition the entropy density drops because of the recombination. However this parameter cannot decrease. Thus implies that the fireball volume must increase by a large factor while the temperature remains approximately constant. Since the growth of the fireball volume takes time the systems spend significant time near  $T_{cr}$ . While the matter hadronizes it's speed of sound  $v_s = \sqrt{\frac{\partial p}{\partial e}}$  is small causing inefficient acceleration that doesn't permit the collective flow increase during this phase.
5. **Chemical freeze-out:** When the temperature decreases enough inelastic interactions among hadrons have completely stopped and only the elastic one occur. This happen because at this point the matter becomes so dilute that the average distance between hadrons exceeds the range of the strong interactions. The hadrons abundance "freeze out" but the creation of some resonance is still possible but such processes don't change the finally observed chemical composition. Since most of the hadrons in a relativistic fireball are pions, very light particle  $m_\pi \sim 140$  MeV, resonances with them are very efficient in keeping the system in thermal equilibrium. The chemical freeze-out occur when  $T = T_{ch}$
6. **Kinetic freeze-out:** At this stage the hadrons, including the unstable resonances, start to decouple from the medium as the temperature lowers and the mean free path becomes larger than the mean distance between hadrons. This mean that particles are no longer subject to significant interactions and can travel freely to the detector. The distribution of kinetic energy among all hadrons has now ceased and the transverse momentum spectrum is approximately exponential while the unstable resonances decay in particle with smaller transverse momenta. Given that the majority of resonances decay by emitting pion, this effect is of particular importance for their spectra, which at low transverse

momenta are dominated by decay products. The kinetic freeze-out occurs when  $T = T_{kin} \sim 153$  MeV. The particles then travel towards the ALICE detector, where they are measured at  $t \sim 10^{15}$  fm/c after the initial collision.

A graphical resume of the process is visible in Fig 2.6 and 2.5

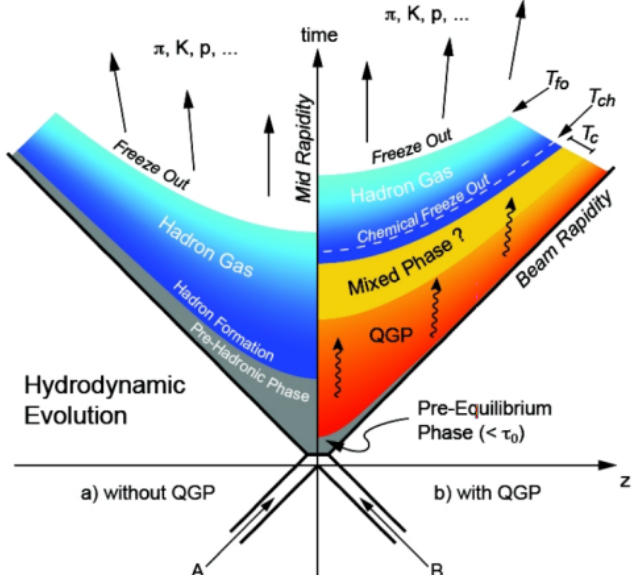


Figure 2.5: Evolution of a central heavy ion collision in a Minkowski-like plane. The two scenarios with and without QGP are pointed out. The critical temperature is indicated by  $T_c$ , while the freeze-out and chemical freeze-out temperatures, are pointed out with  $T_{fo}$ , and  $T_{ch}$ , respectively [1].

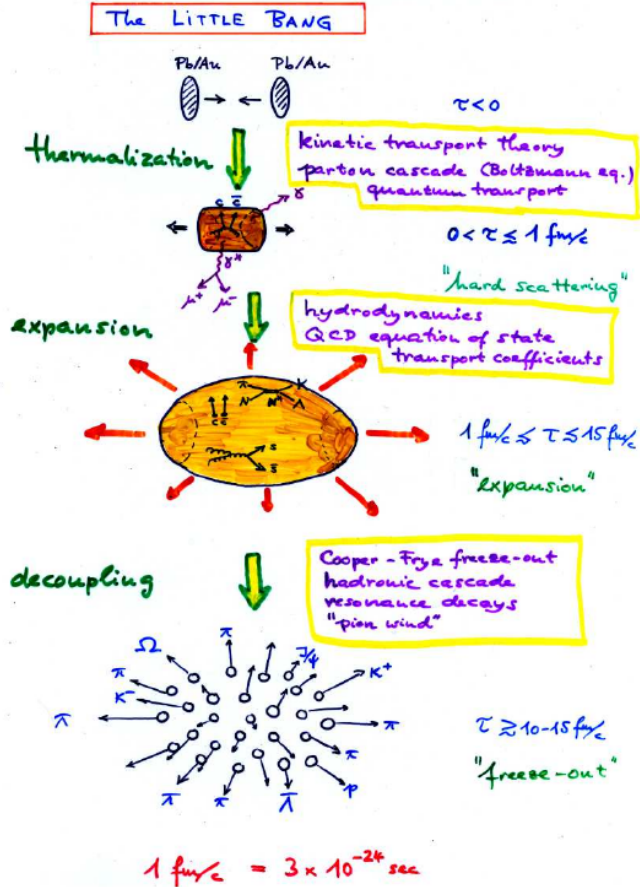


Figure 2.6: A sketched view of the phase of the system after the collision [20].

## 2.0.4 Centrality

An important parameter to characterize heavy-ion collisions is the centrality, which is an observable related to the transverse distance ( $\vec{b}$ ) between the centers of the colliding nuclei. The interaction with the smallest  $|\vec{b}|$  are called central collisions, instead the one with large  $|\vec{b}|$  are called peripheral collisions. Is expressed in therm of the fraction of the total hadronic cross section  $\sigma_{AA}$ . The centrality percentile of collisions with impact parameter ranging in the interval  $[b_1, b_2]$  is given by

$$c(b_1, b_2) = \frac{\int_{b_1}^{b_2} db \frac{d\sigma}{db}}{\int_0^\infty db \frac{d\sigma}{db}} = \frac{\int_{b_1}^{b_2} db \frac{d\sigma}{db}}{\sigma_{AA}} \quad (2.9)$$

The centrality has important consequence in the particle abundances expected, in particular in the number of the charged one. The total number of charged particles produced in a collision is a frequently used observable called multiplicity. For these reason the centrality can be obtain experimentally starting from the measure of the multiplicity or by counting the number

of spectator nucleons, the nucleons that non interact during the collision. The centrality of each collision has to be determined experimentally in order identify peculiar behavior that can arise for very specific centrality classes. Is interesting to report that only 5% of the total cross section correspond to central interaction. [22] The centrality can be used for calculate the number of interacting (participant) nucleons  $N_{part}(b)$  and the total number of binary nucleon-nucleon collisions  $N_{coll}(b)$ . The Glauber Model formulation [29] assumed that: the nucleons are supposed to be point-like and independent, their trajectory is a straight line, the nucleon-nucleon inelastic cross-section does not vary during the collision. All these hypothesis goes under the name of optical limit. Calling A and B the nucleons number respectively in the first and in the second nucleus the probability of having n nucleon-nucleon interactions is given by the binomial distribution.

$$p(n, \vec{b}) = \binom{AB}{n} \left[ T_{AB}(\vec{b}) \sigma_{inzel}^{NN} \right]^n \left[ 1 - T_{AB}(\vec{b}) \sigma_{inzel}^{NN} \right]^{AB-n} \quad (2.10)$$

Where  $\sigma_{NN}$  is the cross section and  $T_{AB}$  is the nuclear overlapping function, it can be computed from the single nucleon distribution of the interacting nuclei. It's possible to imagine this parameter as probability to have a nucleon at the same position in the transverse plane in both colliding nuclei. From the mean value of the binomial.

$$\langle N_{coll}(b) \rangle = A B T_{AB}(\vec{b}) \sigma_{inzel}^{NN} \quad (2.11)$$

So the number of participant is given by:

$$\begin{aligned} \langle N_{part}(\vec{b}) \rangle &= A \int d^2 s T_A(\vec{s}) \left[ 1 - \left( 1 - T_B(\vec{b} - \vec{s}) \sigma_{inzel}^{NN} \right)^B \right] \\ &\quad + B \int d^2 s T_B(\vec{b} - \vec{s}) \left[ 1 - \left( 1 - T_A(\vec{s}) \sigma_{inzel}^{NN} \right)^A \right] \end{aligned} \quad (2.12)$$

With T the thickness function [8].



# Chapter 3

## Thermal model

### 3.0.1 Hydrodynamical description

This section resume the information of [20], [39].

We have already seen that the fireball can be approximately described as an ideal fluid. This approximation hold if the microscopic scattering time scale is much shorter than any macroscopic time scale associated with the fireball evolution. So hydrodynamics becomes applicable when the mean free path of the particles is much smaller than the system size. For these reason the fact that the QGP behaves like an ideal fluid implies strong non-perturbative interactions in the quark-gluon plasma phase. Hydrodynamics allows a description of the system in terms of macroscopic quantities. For these reason an equation that connect the pressure, the energy density and baryon density i.e. an equation of state is required. Lattice QCD suggest a simplify equation of state for an ideal massless gas.

$$P_{pressure} = \frac{\epsilon}{3} = \frac{d\pi^2 T^4}{90} \quad (3.1)$$

where  $d$  is the effective number of degrees of freedom, value of  $d = 47.5$  for a three flavor QGP which is an order of magnitude larger than that of a pion gas where  $d \sim 3$ . [43]

The possibilities to describe the evolution of the fireball in terms of macroscopic quantities make hydrodynamics the ideal language because it allows ad description of the hadronization phase transition without any need for a microscopic description and at the same time explain the observed collective flow phenomena.

The particles velocities in the fireball are under the effect of pressure gradients and are not independent. For these reason in the final state particle velocities will not be distributed according to random thermal motion, but instead will keep a collective ones. This means that, as happen in an expanding gas, the momentum distribution of particles depend on the position in the plasma and is not completely randomical. This feature is commonly called “collective flow” as opposed to the “non-collective flow” in which particles

show uncorrelated velocities. For define the collective flow we can consider any space-time point in the fireball and considered an infinitesimal volume associate with the point. So the flow velocity can be expressed by  $\vec{v}(x) = \frac{|\vec{P}|}{P^0}$ , where  $\vec{P}$  is the mean 3-momentum of the particle in the volume and  $P^0$  is the mean energy in quadrivectorial formalism. It's possible to associate at  $\vec{v}(x)$  a normalized velocity  $u^\mu = \gamma(1, \vec{v}(x))$  where  $\gamma$  is the Lorentz factor. In the same manner we can define  $T(x)$  the average local temperature and the  $\mu_i$ , the chemical potential of the i-th particle species. It's possible to separate the flow velocity into its components along the beam direction (“longitudinal flow”  $\vec{v}_l(x)$ ) and in the plane perpendicular to the beam (“transverse flow”  $\vec{v}_\perp(x)$ ). From now on the natural unit will be used. In this case the phase-space distribution of particles of type i is given by the Lorentz covariant local equilibrium distribution.

$$f_{i,eq}(x, p) = \frac{g_i}{e^{(p \cdot u - \mu_i)/T} + \theta_i} = g_i \sum_{n=1}^{\infty} (\theta_i)^n e^{n(p \cdot u - \mu_i)/T} \quad (3.2)$$

Here  $g_i$  is a spin-isospin-color-flavor-etc. degeneracy factor which counts all particles with the same properties. The factor  $p \cdot u$ <sup>[1]</sup> is the energy of the particle in the local rest frame. The  $\theta_i$  in the denominator accounts for the proper quantum statistics of particle (+1 for fermions and -1 for boson). The Boltzmann approximation corresponds to keeping only the first term in the sum in the last expression. In our applications this is an excellent analytical approximation for all hadrons except for the pion because of their mass.

At relativistic energies it is convenient to parametrize the longitudinal flow velocities and momenta in terms of rapidities and pseudo-rapidities,  $\eta = \frac{1}{2} \ln \frac{1+v}{1-v}$  in this way  $v = \tanh(\eta)$ . It's also possible to define  $\eta_l = \frac{1}{2} \ln \frac{1+v_l}{1-v_l}$  and  $y = \frac{1}{2} \ln \frac{1+\frac{p_l}{E}}{1-\frac{p_l}{E}} = \frac{1}{2} \ln \frac{E+p_l}{E-p_l}$ . Rapidities have the advantage over longitudinal velocities that they are additive under longitudinal boosts. In fact is possible to express  $\eta_l$  in a given inertial frame which moves relative to the first frame with rapidity  $\Delta\eta$  in the -z direction has  $\eta'_l = \eta_l + \Delta\eta$ . In addition the previous expression simplified:

$$u^\mu = \gamma_\perp(\cosh \eta_l, v_x, v_y, \sinh \eta_l) \quad (3.3)$$

$$p^\mu = (m_\perp \cosh y, v_x, v_y, m_\perp \sinh y) \quad (3.4)$$

---

<sup>1</sup>this expression correspond to the quadrivectorial scalar product with the metrical tensor  $P^\mu u_\mu = g^{\mu\nu} P^\mu u^\mu$

$$g_{\mu\nu} = \begin{pmatrix} 1 & 0 & 0 & 0 \\ 0 & -1 & 0 & 0 \\ 0 & 0 & -1 & 0 \\ 0 & 0 & 0 & -1 \end{pmatrix}$$

Where  $\gamma_{\perp} = \frac{1}{\sqrt{1-v_{\perp}^2}}$  and  $m_{\perp} = \sqrt{m^2 + p_{\perp}^2}$  is the transverse mass. For convenience we define also  $\tau = \sqrt{t^2 - z^2}$ , the longitudinal proper time and  $z$  the longitudinal position, and  $\vec{r}_{\perp} = (x, y)$ .

Bjorken argued that at asymptotically high energies the physics of secondary particle production should be independent of the longitudinal reference frame. Furthermore, the boost-invariance of these initial conditions is preserved in longitudinal proper time if the system expands collectively along the longitudinal direction, in this approximation hold  $\eta = \eta_l$ . For more detail see [11]. The Bjorken scaling approximation is expected to be good at high energies and not too close to the beam and target rapidities. We can so said that

$$p \cdot u(x) = \gamma_{\perp}(\vec{r}_{\perp}, \tau) (m_{\perp} \cosh(y - \eta) - \vec{p}_{\perp} \cdot \vec{v}_{\perp}(\vec{r}_{\perp}, \tau)) \quad (3.5)$$

### The Cooper-Frye formula

In this section we will discuss a formalism for count the total number of particles of species  $i$  produced in the collision. Since this value does not depend on the reference frame of the observer, we must be able to express it in a Lorentz-invariant way. We define a three-dimensional hypersurface  $\Sigma(x)$  in 4-dimensional space-time along which we perform the counting. It's clear that different choices for the hypersurface are possible and the final result must not change as long as it completely closes off the future light cone emerging from the collision point. So for obtaining the count of total particle of each species produced we can study how many particles cross the surface. A possible way for obtain the desired result consist in subdividing the hypersurface into infinitesimal elements  $d^3\sigma$  and then summing on them. Defining an outward-pointing 4-vector  $d^3\sigma_{\mu}(x)$  perpendicular to  $\Sigma(x)$  at point  $x$  with the magnitude  $d^3\sigma$ . Introducing the 4-vector  $j_i^{\mu}$  describing the current of particles  $i$  through point  $x$ , and summing over all the infinitesimal hypersurface elements we get

$$N_i = \int_{\Sigma} d^3\sigma_{\mu}(x) j_i^{\mu}(x) = \int_{\Sigma} d^3\sigma_{\mu}(x) \left( \frac{1}{(2\pi)^3} \int \frac{d^3p}{E} p^{\mu} f_i(x, p) \right) \quad (3.6)$$

Where  $j_i^{\mu}(x)$  is the particle number current density given in terms of the Lorentz-invariant phase-space distribution. The normal vector can be computed assuming longitudinal boost-invariance, the freeze-out surface can be characterized by a longitudinal proper time. It's possible to proof that

$$d^3\sigma_{\mu} = \left( \cosh \eta, -\frac{\partial \tau_f}{\partial x}, -\frac{\partial \tau_f}{\partial y}, \sinh \eta \right) \tau_f d^2 r_{\perp} d\eta \quad (3.7)$$

If the freeze-out surface is  $\Sigma_f = (t_f, x_f, y_f, z_f) = (\tau_f \cosh \eta, \vec{r}_{\perp}, \tau_f \sin \eta)$  By multiplying the latter parameters with the velocity  $\frac{p^{\mu}}{E}$  and integrating over

all momenta with measure  $\frac{d^3 p}{(2\hbar\pi)^3} = \frac{d^3 p}{(2\pi)^3}$ . We finally obtain the Cooper-Frye formula

$$\boxed{E \frac{dN_i}{d^3 p} = \frac{dN_i}{dy p_\perp dp_\perp d\phi_p} = \frac{dN_i}{dy m_\perp dm_\perp d\phi_p} = \frac{1}{(2\pi)^3} \int_{\Sigma} p \cdot d^3 \sigma_{\mu}(x) f_i(x, p)} \quad (3.8)$$

With  $\phi_p$  is the azimuthal angle. Combing the Eq 3.7 and 3.5 one get

$$p \cdot d^3 \sigma_{\mu} = (m_\perp \cosh(y - \eta) - \vec{p}_\perp \cdot \nabla_{\perp} \tau_f(\vec{r}_\perp)) \tau_f d^2 r_\perp d\eta \quad (3.9)$$

To compute the measured momentum spectrum we can therefore replace the surface  $\Sigma$  by shrinking it to the smallest and earliest surface that still encloses all the processes. it is called the “surface of last scattering” or “freeze-out surface”  $\Sigma_f$ . The the number of particles obtained from the Cooper-Frye formula is not always positive-definite. Physically negative contributions of the Cooper-Frye formula correspond to particles that stream backwards into the hydrodynamical region. It’s possible to compare the negative contribution with the total number particles crossing the transition hypersurface. It is found that the number of underlying inward crossings is much smaller than the one the Cooper-Frye formula gives under the assumption of equilibrium distribution functions. [33]

To compute the measured momentum spectrum the knowledge of the phase-space distribution on the surface of last scattering is required. Since the transition from strong coupling to free-steaming thus happens in a short time interval we may approximate  $f_i(x, p)$  on the last scattering surface. In this section we report only the final momentum distribution obtainable form the Eq 3.8 result but the proof could be find in the appendix A.

$$\begin{aligned} \frac{dN_i}{dy m_\perp dm_\perp d\phi_p} &= \frac{g_i}{\pi} \int_0^\infty r_\perp dr_\perp n_i(r_\perp) \left[ m_\perp K_1 \left( \frac{m_\perp \cosh(\rho(r_\perp))}{T(r_\perp)} \right) \right. \\ &\quad I_0 \left( \frac{p_\perp \sinh(\rho(r_\perp))}{T(r_\perp)} \right) - p_\perp \frac{\partial \tau_f}{\partial r_\perp} K_0 \left( \frac{m_\perp \cosh(\rho(r_\perp))}{T(r_\perp)} \right) \\ &\quad \left. I_1 \left( \frac{p_\perp \sinh(\rho(r_\perp))}{T(r_\perp)} \right) \right] \end{aligned} \quad (3.10)$$

Where appear the modified Bessel functions and  $v_\perp = \tanh \rho$ . This formula is useful because it allows to easily perform systematic studies of the influence of the radial profiles of temperature, density and transverse flow on the transverse momentum spectrum, in order to better understand which features of a real dynamical calculation of these profiles control the shape of the observed spectra.

Eq 3.10 can be simplified by assuming instantaneous freeze-out. In this case there is no dependence of the proper time at the freeze-out surface  $\tau$  therefore  $\frac{\partial \tau}{\partial r_\perp} = 0$  so we can rewrite the previous equation in the following manner.

$$\frac{dN_i}{dy m_\perp dm_\perp} = \frac{g_i}{\pi^2} \int_0^\infty r_\perp dr_\perp n_i(r_\perp) \left[ m_\perp K_1 \left( \frac{m_\perp \cosh(\rho(r_\perp))}{T(r_\perp)} \right) I_0 \left( \frac{p_\perp \sinh(\rho(r_\perp))}{T(r_\perp)} \right) \right] \quad (3.11)$$

Commonly named Boltzmann-Gibbs blast wave. This formulation is particularly used for extract properties of the common source such as the temperature  $T_f$  or to fit the single particle spectra. The agreement of Eq 3.11 with the spectra is quite remarkable especially in central events where the thermal description is expected to work better. However for a more precise description some models take into account also the final state interaction effects, such as the Coulomb repulsion/attraction between charged hadrons which continues long after their strong interactions with each other have ceased.

### Transverse momentum spectra and freeze-out temperature

For all hadrons is observed that  $m_\perp/T > 1$  so the modified Bessel function can be approximate in the following manner  $K_\nu \sim e^{-\frac{m_\perp \cosh \rho}{T}}$ . At  $r_\perp = 0$  the radial flow velocity must vanish by symmetry but to larger  $r_\perp$  typically rises linearly, it eventually reaches a maximum value and drops again to zero since the dilute tail of the initial density distribution freezes out early. Some simulated profile of grow are shown in the Fig 3.1 [45].

Different process can manifest, for example at SPS energies the freeze-out surface moves from the edge inward since the fireball matter cools and freezes out faster than the developing radial flow can push it out. At LHC energies the much stronger radial flow generated by the much higher internal pressure makes the fireball grow considerably arriving at radius of 13 fm/c. For understand how the radial flow influence the spectra first consider the absence of flow ( $\rho = 0$ ), in this condition  $I_q(0) = 0$  so the Eq 3.10 reduced to

$$\frac{dN_i}{dy m_\perp dm_\perp} \sim m_\perp K_1 \left( \frac{m_\perp}{T} \right) \sim m_\perp^{1/2} e^{-\frac{m_\perp}{T}} \quad (3.12)$$

In these condition as the temperature is the same for all hadron the spectra depend only on the transverse mass, a fact known as "  $m_\perp$  " scaling. As visible in the equation the temperature can be extracted easily. Instead if the radial flow is not vanishing approximating  $p_\perp \approx m_\perp$  one get.

$$\frac{dN_i}{dy m_\perp dm_\perp} \sim e^{-\frac{m_\perp (\cosh \rho - \sinh \rho)}{T}} = e^{-\frac{m_\perp}{T_{slope}}} \quad (3.13)$$

With  $T_{slope} = T \sqrt{\frac{1+v_\perp}{1-v_\perp}}$ . Convective flow breaks  $m_\perp$  scaling especially at low  $m_\perp$  as in Fig 3.2. In fact for sufficiently large hadron mass and flow velocity

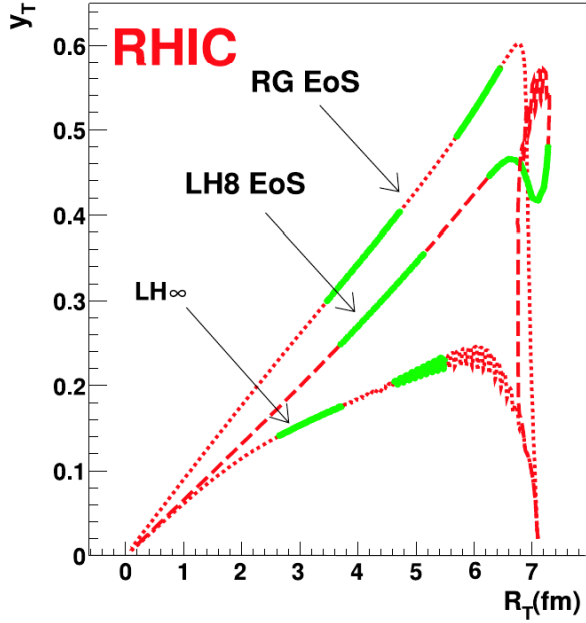


Figure 3.1: Radial flow rapidity profile  $\rho(r_\perp) = y_T$  for central Au+Au collisions at RHIC, from hydrodynamic calculations employing three different equations of state [1].

the spectrum develops a blast wave peak at nonzero transverse momentum. In conclusion is possible to summarize these two important limits

$$\text{Non relativistic: } p_\perp \ll m_i \quad T_{i,\text{slope}} \approx T_f + \frac{1}{2}m_i\langle v_\perp \rangle^2 \quad (3.14)$$

$$\text{Relativistic: } p_\perp \gg m_i \quad T_{\text{slope}} = T \sqrt{\frac{1+v_\perp}{1-v_\perp}} \quad (3.15)$$

This effect are visible in Fig. 3.2 for two flow velocities. These formulations have of course their practical limitations in fact pions, the lightest hadrons, are quickly falling into the relativistic case and few measure are performed at low momenta, especially in collider experiments. In addition, non-relativistic pions are affected by both Bose-Einstein statistics and contribution from resonance decays. Furthermore the  $m_\perp$ -scaling is expected to be more evident for the pp collision while for the heavy-ion case the presence of the radial flow breaks the  $m_\perp$ -scaling. The modification of the spectral shape affects also the mean of the distribution in a mass-dependent way, resulting in an increase of the  $p_\perp$  with the particle mass. This increasing is expected to be more evident when flow is stronger.

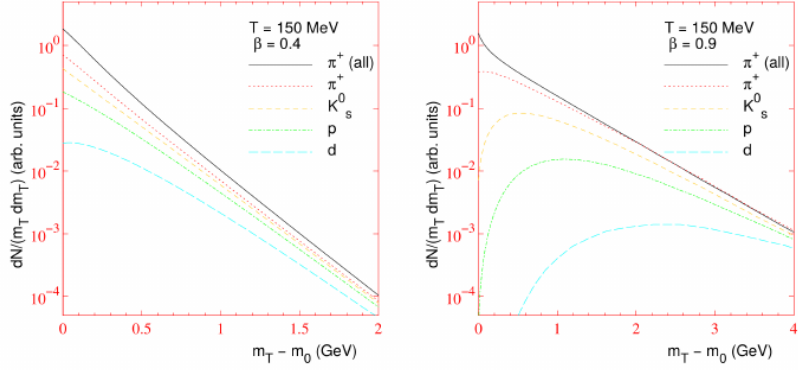


Figure 3.2: Flow spectra for various hadrons as a function of  $m_{\perp} - m_0$  where  $m_0$  is their rest mass. The calculation assumes an infinitesimally thin shell of temperature  $T = 150$  MeV expanding with  $v_{\perp} = 0.9$ . The curve labelled "π<sup>+</sup> (all)" includes pions from resonance decays in addition to the thermally emitted pions.

### 3.0.2 Anisotropic flow

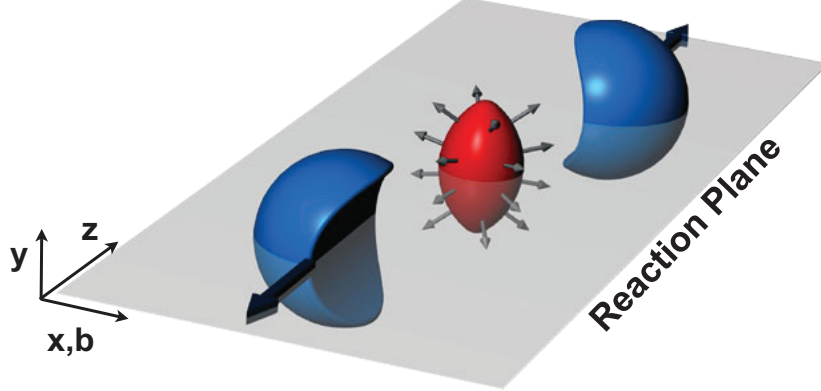


Figure 3.3: Almond shaped interaction volume after a non-central collision of two nuclei. The spatial anisotropy with respect to the x-z plane (reaction plane) translates into a momentum anisotropy of the produced particles (anisotropic flow).

This section come from [43], [20] [25]. For central collisions between equal spherical nuclei, radial flow is the only possible type of transverse flow allowed by symmetry. In non-central collisions, however, this azimuthal symmetry is broken, and anisotropic transverse flow patterns can develop. Experimentally, anisotropic flow provides the most direct evidence of flow in the QGP, producing anisotropy in particle momentum distributions. The evolution of the elliptic shaped interaction volume is shown in Fig 3.4 [24]. The contours indicate the energy density profile and the sequence show time evolution from an almost elliptical region into an almost symmetric system, an expansion

that happen at the speed of sound. In this situation the equation 3.8 can be

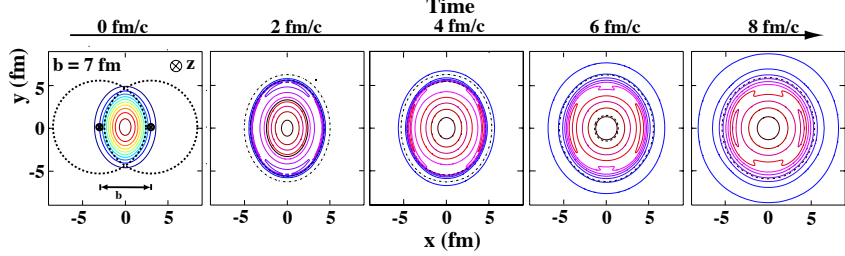


Figure 3.4: The created initial transverse energy density profile and its time dependence in coordinate space for a non-central heavy-ion collision. The z-axis is along the colliding beams, the x-axis is defined by the impact parameter.

written using a Fourier expansion introducing  $b$ , the impact parameter, and  $\psi_n$  the azimuthal angle, in the form

$$\begin{aligned} E \frac{dN_i}{d^3p}(b) &= \frac{dN_i}{dy p_\perp dp_\perp d\phi_p}(b) \\ &= \frac{1}{2\pi} \frac{dN_i}{dy p_\perp dp_\perp}(b) \left( 1 + 2 \sum_{n=1}^{\infty} v_n^i(p_\perp, b) \cos(n(\phi_p - \psi_n)) \right) \end{aligned} \quad (3.16)$$

In this Fourier decomposition, the coefficients  $v_1$ ,  $v_2$  and  $v_3$  are known as directed, elliptic and triangular flow respectively. As visible in Fig 3.3 the momentum space distribution has a preferred direction and this asymmetry can be quantified by the spatial ellipticity:

$$\epsilon_x(b) = \frac{\langle y^2 - x^2 \rangle}{\langle y^2 + x^2 \rangle} \quad (3.17)$$

As a function of time,  $\epsilon_x$  decreases spontaneously due to the free-streaming radial expansion, in the absence of rescattering, or faster due to the development of elliptical flow if rescattering does occur. The first mechanism is a consequence of the Heisenberg uncertainty principle because if the definition in the position increase the uncertainty on the linear momentum in the same direction make the same. Instead the elliptic flow is a consequence of the fact that there is high pressure in the interior of the reaction zone which falls off to zero outside. The pressure gradient is very steep in the short direction leading a stronger hydrodynamic acceleration. It's possible to show that the spatial eccentricity decrease as a function of time in the following manner, the proof is in the appendix B.

$$\frac{\epsilon_x(\tau_0 + \Delta\tau)}{\epsilon_x(\tau_0)} = \left[ 1 + \frac{(c\Delta\tau)^2}{\langle \vec{r}^2 \rangle_{\tau_0}} \right]^{-1} \quad (3.18)$$

where  $\tau_0$  is the time when the particles were created and  $\langle \vec{r}^2 \rangle_{\tau_0}$  is the azimuthally averaged initial transverse radius squared of the reaction zone. Hydrodynamics predicts that heavier particles gain more momentum than lighter

ones for the previously discussed flattening of their spectra at low transverse kinetic energies. It is also known from microscopic kinetic studies that for a given initial spatial eccentricity the magnitude of the generated elliptic flow is a monotonic function of the mean free path.

More recently, it was realized that small deviations from ideal hydrodynamics, in particular viscous corrections, modify significantly the buildup of the elliptic flow. The shear viscosity determines how good a fluid is, however, for relativistic fluids the more useful quantity is the shear viscosity over entropy ratio  $\eta_v/s$ . For perfect fluids the ratio can be approximated by:

$$\frac{\eta_v}{s} \approx \frac{\hbar}{4\pi k_B} \quad (3.19)$$

It is argued that the transition from hadrons to quarks and gluons occurs in the vicinity of the minimum in  $\eta_v/s$ , just as in the phase transitions of common life substances such as water.

### 3.0.3 Statistical Hadronisation Model (SHM)

This section had been inspired by the folowing article [9], [7] [20] [22].

The idea of applying statistical concepts to the problem of multi-particle production in high energy collisions dates back to a work of Fermi in 1950, who assumed that particles originated from an excited region evenly occupying all available phase space states. Note that such a statistical approach has, of course, its limitations. In fact in this way is impossible to investigate correlations between pairs, triplets, quadruplets etc. of particles because they belong to the same event and so are not produced entirely independently but correlated in a non-statistical way. For example the momenta of the particles emerged from the fireball must conserve the original one of the initially colliding nuclei generating non-statistical correlations. So for describe this complex dynamical process, the Statistical Hadronisation Model (SHM) postulates that hadrons are formed from the decay of each cluster in a purely statistical way so. *Every multihadronic state localized within the cluster and compatible with conservation laws is equally likely.*

Often the mathematical formalism used to describe the system is the grand-canonical one, which takes into account the possibility for the volume under study to exchange both particles and energy with its surroundings. This approach is justified by the fact that in heavy-ion collisions the volume of the fireball is considerably larger than the partonic scale; indeed, the volume of clusters is in constant ratio to their mass when hadronisation takes place. For smaller systems, like happen for example in collision between proton or proton and other nucleus, the grand-canonical ensemble is no longer a good description of the system. In this case the volume created after the collision is considerably smaller and it is better to require the local conservation of quantum numbers and so the canonical formulation is more appropriate. It

is worth noting that the transition from a canonical to a grand-canonical description effectively occurs when the cluster volume is of the order of  $100 \text{ fm}^3$  at an energy density of  $0.5 \text{ GeV/fm}^3$  [23]. In addition one has to consider the quantum behaviour of both fermionic and bosonic degrees of freedom that form the system. Some possible effect are for example the Bose-Einstein correlations or Hanbury Brown-Twiss interference. The Bose-Einstein correlations refer to a quantum mechanical phenomenon that arises due to the wave-like nature of bosonic particles and their tendency to occupy the same quantum state. Instead the Hanbury Brown and Twiss effect is any of a variety of correlation and anti-correlation effects in the intensities received by two detectors from a beam of particles and depend on the fermionic or bosonic nature of the beam. From statistical mechanics is known that hold

$$\langle N \rangle = \frac{1}{\beta} \left( \frac{\partial \ln Z}{\partial \mu_B} \right) \quad (3.20)$$

$$\langle E \rangle = - \left( \frac{\partial \ln Z}{\partial \beta} \right) + \mu_B \langle N \rangle \quad (3.21)$$

$$\langle S \rangle = k_B \frac{\partial T \cdot \ln Z}{\partial T} \quad (3.22)$$

$$P_{pressure} = \frac{1}{\beta} \left( \frac{\partial \ln Z}{\partial V} \right) \quad (3.23)$$

Where  $E, S, P_{pressure}, N, T$  and  $k_B$  are respectively the energy, the entropy, the pressure, the number of particle the temperature and the Boltzmann constant, instead  $\beta = \frac{1}{k_B T}$  and  $Z$  is the partition function that can be expressed in the following manner

$$\ln Z_i(T, V, \mu_i) = \frac{\Delta V g_i}{2\pi^2 \hbar^3} \int_0^\infty \theta_i p^2 \, dp \ln(1 + \theta_i e^{\beta(\mu_i - E)}) \quad (3.24)$$

$\theta_i$ , already define, is +1 for fermions and -1 for bosons and  $g_i$  the overall degeneracy. Global observables such as the particle mean multiplicities and entropy can be derived from the previous equation:

$$\langle N \rangle = \frac{\Delta V g_i}{2\pi^2 \hbar^3} \int_0^\infty dp \frac{p^2}{e^{-\beta(\mu_i - E)} + \theta_i} \quad (3.25)$$

$$\langle S \rangle = - \sum_i \int_{\Delta V} \int \frac{d^3x d^3p}{(2\pi)^3} [f_i \ln f_i + \theta_i (1 - \theta_i f_i) \ln(1 - \theta_i f_i)] \quad (3.26)$$

In this case the distribution is a bit different from the 3.2.

$$f_{i,eq}(x, p) = \frac{g_i}{e^{\beta(\Delta V)(E_i - \mu_i(\Delta V))} + \theta_i} \quad (3.27)$$

The Eq 3.24 can be further developed by considering Taylor expansion of the logarithmic part, the full derivation is given in the appendix C.

$$\ln Z_i(T, V, \mu_i) = \frac{\Delta V g_i}{2\pi^2 \hbar^3 \beta} \sum_K \frac{(\theta_i e^{\beta \mu_i})^k}{k^2} m_i^2 K_2(k\beta m_i) \quad (3.28)$$

The definition of the chemical potential  $\mu_i$  is strictly related to the processes under study and to the type of chosen ensemble formalism. It became necessary in order to take into account the possibility to have fluctuations of the number of particles of species i. For a given species i the chemical potential can be split into  $\mu_i = B_i \mu_B + S_i \mu_S + Q_i \mu_Q$ , where  $B_i$ ,  $S_i$  and  $Q_i$  are respectively the baryon number, strangeness and electric charge while  $\mu_B$ ,  $\mu_S$  and  $\mu_Q$  are the corresponding chemical potentials. If the energy of the collision is not enough the strange quark and antiquark can be non thermalized. So we should add another term to chemical potential, This term take the form  $|s_i| \bar{\mu}_s$  where  $s_i$  is the total number of strange quarks and antiquarks in hadron and  $\bar{\mu}_s$  the corresponding potential. However in heavy-ion collisions the s quarks can be fully thermalized. Similarly as in the case of the strange quark, it is then possible to repeat the same operation for the heavier flavours.

Starting from measurements of the identified particle yields ( $dN/dy$ ) in the light flavor sector by using the SHM approach one gains access to the thermodynamic properties of the system created in the collision. An example of such measurement for different particle species is given in Fig. 3.5. It is possible to see that the large evolution in particle production and identify some key features:

- Particles and antiparticles tend to be equally produced if the collision energy is high enough. This is especially true at LHC energies.
- Baryons and mesons follow different behaviour with significant baryon/anti-baryon discrepancies at lower energies.
- Pions are the most abundant particle species produced
- Particles containing s or c quarks are subject to a significant increase in their abundances at opportune energy. This effect known as “strangeness enhancement” was historically identified as a signature typical of the QGP. This aspect will be discuss better later.
- At high energies the production of particles with same mass but different quark content tends to be similar.

The SHM can be used to fit the measured  $dN/dy$  using only a limited number of parameters. This allows to obtain quantities such as the chemical freeze-out temperature, the system volume V and the chemical potential  $\mu_B$ . Results Fig. 3.6 show how the best fit parameters to describe the data from Pb–Pb central collisions collected by the ALICE experiment at  $\sqrt{s_{NN}} = 2.76$

TeV are:  $T = 156.5 \pm 1.5$  MeV,  $\mu_B = 0.7 \pm 3.8$  MeV,  $V = 5280 \pm 410$  fm<sup>3</sup>. The model is able to describe reasonably well measurements of yields which span over 9 order of magnitudes with a  $\tilde{\chi}^2 = 1.61$  with a low number of free parameters. The largest tension is observed for p and  $\bar{p}$ , reaching almost a 3  $\sigma$  deviation. [5] In addition these results allow for a direct comparison with predictions from lattice QCD. Such comparison is resumed in Fig. 3.7 where is possible to see that the curve is correctly described.

### 3.0.4 Strangeness and Charmness enhancement

Another success of the SHM model is the prediction of a phenomenon called strangeness enhancement, which consists of an increase in the production of particles containing strange quarks. In particle production, one would generally expect that the heavier flavours should be suppressed compared to the up and down quarks, both for their greater mass and the need to preserve quantum numbers. In fact is known that the strong interactions exactly preserve the strangeness quantum number and so the heavier flavours are produced in pairs. Consequently, the production of strange quarks is expected to be suppressed in small collision systems where there is less phase space available for particle production. This because the creation of a second hadron with a compensating strangeness has to be created inside the same small volume at the same time resulting in a large energetic threshold that the system has to overcome (canonical suppression). Instead the fact that the gran canonical formalism, that assumes only the average conservation of the quantum number, is useful for the description of this kind of process tell us that the system behave as if the strange and antistrange hadrons were created independently and statistically distributed over the entire nuclear fireball. This mean that are not important the initial conditions in witch the pairs  $s\bar{s}$  are created for determine the final distribution. This point is not completely understood but is probably related to the fact that a significant amount of strangeness diffusion occur before hadronization.

In heavy-ion collisions, the enhancement of strange hadron production is possible due to the high gluon density of the QGP. This is thanks to the dominance of gluonic production channels, such as the processes  $gg \rightarrow s\bar{s}$ ,  $u\bar{u} \rightarrow s\bar{s}$  and  $d\bar{d} \rightarrow s\bar{s}$ . In addition, the partial restoration of the chiral symmetry in proximity to the temperature of deconfined transition reduces the constituent mass thus decreasing the energetic threshold for its production. These reduce also the time scale for strangeness saturation that occur for temperatures above 160 MeV, very close to the chemical freeze-out one where the relative particle abundances are fixed. As a consequence when quark-gluon plasma disassembles into hadrons in a breakup process and the larger amount of strange quarks available made particle with this flavour more abundant in the final state.

Instead the charm quark mass is much larger than the other described

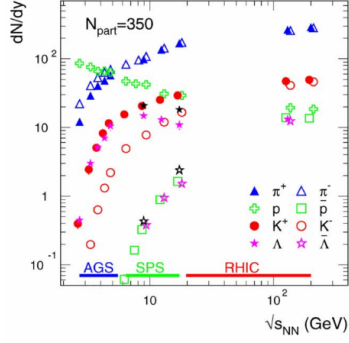


Figure 3.5: The energy dependence of experimental hadron yields at mid-rapidity for various species produced in central nucleus-nucleus collisions. The energy regimes for various accelerators are marked. Note that, for SPS energies, there are two independent measurements available for the  $\Lambda$  hyperon yields. [6]

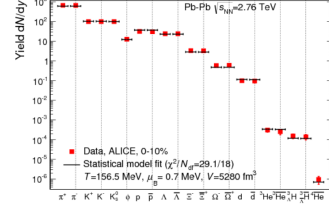


Figure 3.6: adron multiplicities in central (0-10%) Pb–Pb collisions at the LHC, for different particles.[5]

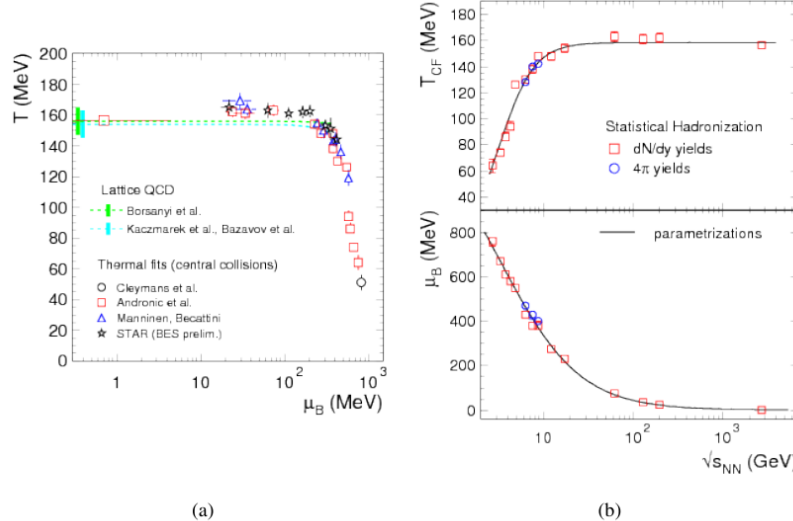


Figure 3.7: The a panel show (a) comparison between the Phase diagram of QCD with data points as obtained at different energies and the thermal model fits from SIS up to LHC data. The panel (b) show the evolution of the temperature of chemical freeze-out and the  $\mu_B$  as a function of the  $\sqrt{s_{NN}}$ .[5]

in this section and hence thermal production of charm quarks or hadrons is strongly suppressed. However, with increasing center-of-mass energy the total charm production cross section, which results from initial hard collisions, increases strongly. In this case similar considerations made for the strange quark holds also for the heavier charm flavor.

# Chapter 4

## $Y_c\mathbf{N}$ bound state

### 4.0.1 One Boson exchange model

Before the publication of Hideki Yukawa's groundbreaking papers in 1935 [52], physicists struggled to explain the results of James Chadwick's atomic model, which proposed that protons and neutrons were packed inside a small nucleus with a radius on the order of  $10^{-14} - 10^{-15}$  meters. At such small scales, the electromagnetic forces would be extremely intense, causing the protons to repel each other. In 1932, Werner Heisenberg proposed a "Platzwechsel" (migration) interaction between protons and neutrons within the nucleus, suggesting that neutrons were composite particles made of protons and electrons. According to this model, neutrons would emit electrons, creating an attractive force with protons, and then transform back into protons [28]. However, this model violated the conservation of linear and angular momentum. To resolve this issue, Enrico Fermi proposed in 1934 that the emission and absorption of two light particles: the neutrino and electron. A few months later, Soviet physicists Igor Tamm and Dmitri Ivanenko demonstrated that the force associated with the emission of neutrinos and electrons was not strong enough to bind protons and neutrons together in the nucleus.

Yukawa decides so to combine both the idea of short-range force interaction and the idea of an exchange particle in order to explain the neutron-proton binding. For introduce the Yukawa's potential is possible to start from the Klein-Gordon equation that governs dynamics of free massive scalar, without spin, field

$$\nabla^2 \phi(\vec{r}, t) - \frac{1}{c^2} \frac{\partial^2 \phi(\vec{r}, t)}{\partial^2 t} = \frac{m^2 c^2}{\hbar^2} \phi(\vec{r}, t) \quad (4.1)$$

where  $\phi$  is the wave function,  $\vec{r}$  the position,  $t$  the time, and  $m$  the mass of the particle. In spherical coordinate becomes for the radial component.

$$\frac{1}{r^2} \frac{\partial}{\partial r} (r^2 \frac{\partial}{\partial r} \phi(\vec{r}, t)) - \frac{1}{c^2} \frac{\partial^2 \phi(\vec{r}, t)}{\partial^2 t} = \frac{m^2 c^2}{\hbar^2} \phi(\vec{r}, t) \quad (4.2)$$

A possible solution is.

$$\phi(\vec{r}, t) = -g^2 \hbar c \frac{e^{\frac{i}{\hbar}(\vec{r} \cdot \vec{P} - Et)}}{r} \quad (4.3)$$

Where  $\vec{P}$  is the linear momentum and E the energy. For virtual particles hold that  $0 \sim p^2 c^2 + m^2 c^4$  so  $p \sim \pm imc$  and with the Einstein-De Broglie equation one get that  $\lambda = \frac{\pm ih}{mc}$ , named Compton wave length, and the solution can be rewritten rejecting the divergent solution as

$$\phi(\vec{r}, t) = -g^2 \hbar c \frac{e^{-\frac{r}{\lambda}}}{r} = -g^2 \hbar c \frac{e^{-\frac{rmc}{\hbar}}}{r} \quad (4.4)$$

The Eq. 4.4 describe how the mediators of the interaction evolve with time clearing that the massive one produces a short-range interaction due to the exponential decrease. A graphical representation of the phenomena is visible in the Fig 4.1.

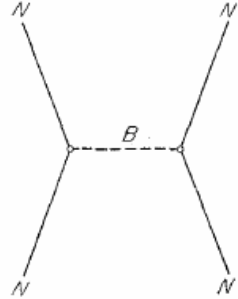


Figure 4.1: The one-boson-exchange diagram of the nucleon-nucleon scattering.

Yukawa used his equation also to predict the mass of the mediating particle in nucleus as about 280 times the mass of the electron  $\sim 140$  Mev. Physicists called this particle the "meson," as its mass was in the middle of the leptons and baryons ones. Yukawa's meson was found in 1947, and came to be known as the pion [13]. This model of interaction based on the exchange of particle is generally called "one-boson-exchange model" (OBE model) or the "one-particle-exchange model". This model has opened up a new possibility for a realistic understanding of nuclear forces; indeed, based on the Yukawa potential, the Sakata model [26] was created with the aim of giving a systematic understanding not only of the nucleon-nucleon interaction but also of other various strong reactions. While the OBE model is extremely useful for understanding the basics of nuclear interactions, it has several important limitations that prevent it from being a complete theory of nuclear forces. [44]. Furthermore, the theory has been extended since Sakata's proposal, and some ideas from the model have been incorporated into QCD. However, his introduction was important for understanding the next section.

### 4.0.2 $\Lambda_c$ N interaction

This section is a resume of the [19] and [27]. As already seen, the construction of a model to describe non-perturbative QCD phenomena with analytical first-principles calculations is very limited. In addition, the lack of experimental information on  $Y_c N$ , a bound state of a particle containing a quark charm, in particular for our issue  $\Lambda_c$ , and a nucleon (N), makes its description much more difficult. The situation can therefore be improved by using well-constrained models based as much as possible on symmetry principles and analogies with other similar processes. For this scope an approach was proposed in the early 1990s in an attempt to obtain a simultaneous description of the light baryon spectrum and the nucleon-nucleon interaction [47]. In this model, baryons are described as clusters of three interacting massive (constituent) quarks and is for these reason called Constituent Quark Model (CQM). In this way the microscopic interaction between quarks and gluons are neglected.

According to Goldstone's theorem, when a continuous symmetry is spontaneously broken, new massless scalar particles appear in the spectrum of possible excitations. These particles are called Goldstone bosons and can be thought as the excitations of the field in the broken symmetry directions in group space. This spinless boson can acquire a mass if the symmetry is not exact, like happen for the approximate chiral symmetry, but they typically remain relatively light if compared to other hadrons like protons and neutrons [42]. When the Goldstone bosons are created in the system they can be exchanged by other particle creating a potential. For the chiral symmetry the Goldstone bosons are pions ( $\pi$ ) and their chiral partner ( $\sigma$ ) and the complessive potential take the form:

$$V_\chi = V_\sigma(\vec{r}_{ij}) + V_\pi(\vec{r}_{ij}) \quad (4.5)$$

where

$$V_\sigma(\vec{r}_{ij}) = \frac{-g_{ch}^2}{4\pi} \frac{\Lambda^2}{\Lambda^2 - m_\sigma^2} m_\sigma \left[ Y(m_\sigma r_{ij} - \frac{\Lambda}{m_\sigma}) Y(\Lambda r_{ij}) \right] \quad (4.6)$$

$$\begin{aligned} V_\pi(\vec{r}_{ij}) &= \frac{g_{ch}^2}{4\pi} \frac{m_\pi^2}{12m_i m_j} \frac{\Lambda^2}{\Lambda^2 - m_\pi^2} m_\pi \left[ Y(m_\pi r_{ij} - \frac{\Lambda^3}{m_\pi^3}) Y(\Lambda r_{ij}) \right] \vec{\sigma}_i \cdot \vec{\sigma}_j \\ &+ \left[ H(m_\pi r_{ij}) - \frac{\Lambda^3}{m_\pi^3} H(\Lambda r_{ij}) \right] S_{ij}^2(\vec{\tau}_i \cdot \vec{\tau}_j) \end{aligned} \quad (4.7)$$

$\frac{g_{ch}^2}{4\pi}$  is the chiral coupling constant,  $m_i$  are the masses of the constituent quarks,  $\Lambda \sim \Lambda_{CSB} = 4\pi f_\pi \sim 1\text{GeV}$  a momentum scale where  $f_\pi$  is the pion electroweak decay constant,  $Y(x) = \frac{e^{-x}}{x}$  is the standard Yukawa function,  $H(x) = (1 + \frac{3}{x} + \frac{3}{x^2})Y(x)$ ,  $S_{ij} = 3(\vec{\sigma}_i \cdot \hat{r}_{ij})(\vec{\sigma}_j \cdot \hat{r}_{ij})\vec{\sigma}_i \cdot \vec{\sigma}_j$  is the quark tensor operator with  $\sigma$  the Pauli matrices. For an explicit expression of the parameter and their expectation value see [27]. The meson exchange potential contains four kinds of terms: spin-independent, spin-spin, spin-orbit, and tensor. The

spin-independent term is the one that has the greatest influence on the depth and shape of the potential well at not too small distances and for these reason it will be studied in bigger detail in the following section. The spin operator also includes the Pauli repulsion in its effect, producing an increasing repulsion as the distance between the hadrons decreases, which became essential for the fermion description. It's possible to see that this term will become significant in determining which configuration between nucleons is most plausible to be observed. The spin-orbit and tensor contributions can instead be thought as effects analogous to magnetism, due to the presence of relative motion in the colour charges (colour-magnetism effect). The latter will then contribute in the case where the total angular momentum of the bound state is not zero. Perturbative QCD effects are taken into account through the one-gluon-exchange (OGE) potential that take the form:

$$V_{OGE}(\vec{r}_{ij}) = \frac{\alpha_s}{4} \vec{\lambda}_i^c \cdot \vec{\lambda}_j^c \left[ \frac{1}{r_{ij}} - \frac{1}{4} \left( \frac{1}{2m_i^2} + \frac{1}{2m_j^2} + \frac{2\vec{\sigma}_i \cdot \vec{\sigma}_j}{3m_i m_j} \right) \frac{e^{-r_{ij}/r_0}}{r_0^2 r_{ij}} \frac{3S_{ij}}{4m_i m_j r_{ij}^3} \right] \quad (4.8)$$

where  $\vec{\lambda}^c$  are the SU(3) color matrices,  $r_0 = \hat{r}_0/\nu$  is a flavor-dependent regularization scaling with the reduced mass  $\nu$  of the interacting pair, and  $\alpha_s$  is the scale-dependent strong coupling constant given by:

$$\alpha_s(\nu) = \frac{\alpha_0}{\ln[(\nu^2 + \mu_0^2)/\gamma_0^2]} \quad (4.9)$$

$\alpha_0=2.118$ ,  $\mu_0 = 36.976$  Mev and  $\gamma_0=0.113$  fm $^{-1}$ . the equation 4.9 give rise  $\alpha_s \sim 0.54$  for light quark and  $\alpha_s \sim 0.43$  for uc pairs. The table resume all the parameter 4.1

$m_{u,d}$ (MeV)	313	$g_{ch}^2/4\pi$	0.54
$m_c$ (MeV)	1752	$m_\sigma$ (fm $^{-1}$ )	3.42
$\hat{r}_0$ (MeV fm)	28.170	$m_\pi$ (fm $^{-1}$ )	0.70
$\mu_c$ (fm $^{-1}$ )	0.70	$\Lambda$ (fm $^{-1}$ )	4.2
$b$ (fm)	0.518	$a_c$ (MeV)	230

Table 4.1: The table summarizes the typical values of the parameters present in the previous equation.

Finally, any model imitating QCD should incorporate confinement. Although it is a very important term from the spectroscopic point of view but it is negligible for the hadron-hadron interaction. Lattice QCD calculations suggest a screening effect on the potential when increasing the interquark distance which is modeled here by.

$$V_{CON}(\vec{r}_{ij}) = -\alpha_c(1 - e^{-\mu_c r_{ij}})\vec{\lambda}_i^c \cdot \vec{\lambda}_j^c \quad (4.10)$$

The figures 4.1 shows the different diagrams contributing to the charmed baryon-nucleon interaction. The first type of interaction, visible in (a) and (b),

is mediated by the exchange of a boson between light quark or between a light ad heavy flavor. The second one instead take in account also the exchange of the identical light quark (c) and (d). The second possibility correspond to short range interaction based on one-gluon exchange contributions not so relevant in the interaction in ordinary nucleus because of the only presence of light flavour. In the limit where the two baryons  $Y_c$  N overlap, the Pauli principle impose antisymmetry requirements. Such effects, if any, will be prominent for relative S waves ( $L = 0$ ). The S wave normalization kernel of the two-baryon wave function can be written in the overlapping region ( $R \rightarrow 0$ )

$$N \rightarrow 4\pi \left( 1 - \frac{R^2}{8} \left( \frac{5}{b^2} + \frac{1}{b_c^2} \right) \right) [1 - 3C(S, I) + \dots] \quad (4.11)$$

Where  $C(S, I)$  is a spin-isospin coefficient and  $b, b_c$  are the parameters for the wave function of the light and charmed quarks, respectively, assumed to be different for the sake of generality. The closer the value of  $C(S, I)$  to  $1/3$  the grater is the suppression at short distances of the wave function, generating Pauli repulsion, effect visible in the phase shift. So there might exist Pauli suppressed channels.

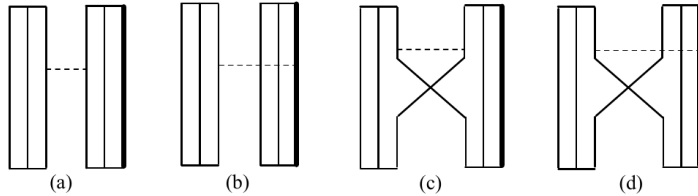


Figure 4.2: The vertical solid lines represent a light quark, u or d. The vertical thick solid lines represent the charm quark. The dotted horizontal lines stand for the exchanged boson. The different type of interaction are: (a) Interaction between two light quarks. (b) Interaction between the heavy and a light quark. (c) Interaction between two light quarks together with the exchange of identical light quarks. (d) Interaction between the heavy and a light quark together with the exchange of identical light quarks.

A numerical simulation of the potential is described in [30], performed with lattice QCD with lattice spacing  $a = 0.0907(13)\text{fm}$  and physical lattice size  $\text{La}=2.902(42)\text{fm}$ . The figure 4.3 shows the  $\Lambda_c N$  central potential in the  $^1S_0$  channel with different masses considered for the pion. For ensemble 1  $m_\pi \sim 700$  Mev,  $m_\pi \sim 570$  Mev for ensemble 2 and 410 Mev for ensemble 3. They found a repulsive interaction at short distances ( $r < 0.5$  fm) and an attractive one for intermediate distances ( $0.5 < r < 1.5$  fm). The same calculation has also been performed with a  $\Lambda_c N$  system with  $J^P = 1^+$  obtaining the result visible in the figure 4.4, The two result are qualitatively and quantitatively similar except at short distance ( $r < 0.5$  fm). As can be seen for both  $\Lambda_c N$  S waves the intensity of the attraction becomes stronger as the

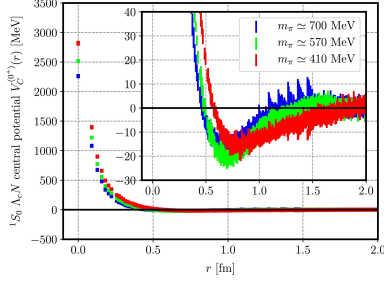


Figure 4.3: The figure show  $\Lambda_c N$  central potential in the  $^1S_0$  channel for each ensemble. The potential is calculated for  $m_\pi \approx 700$  MeV case (Blue), for  $m_\pi \approx 570$  MeV case (Green) and for  $m_\pi \approx 410$  MeV case (Red).

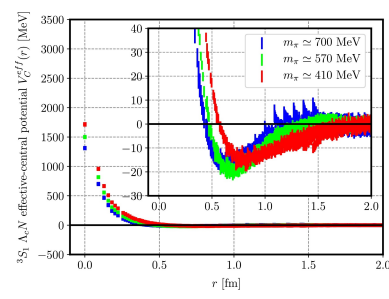


Figure 4.4: The figure show  $\Lambda_c N$  central potential in the  $^3S_1$  channel for each ensemble. The potential is calculated for  $m_\pi \approx 700$  MeV case (Blue), for  $m_\pi \approx 570$  MeV case (Green) and for  $m_\pi \approx 410$  MeV case (Red).

pion mass decreases, moving towards the predictions of the CQM. However the  $^3S_1$  potential is more attractive than  $^1S_0$ . This is due to the short-range dynamics consequence of gluon and quark exchange. In fact, if no meson exchanges were considered, the S wave phase shifts of the  $\Lambda_c N$  system are very similar to the corresponding NN scattering. Instead considering the exchange both partial waves are subjected by hard-core phase shifts due to the short-range gluon and quark-exchange dynamics. However, the hard-core radius in the spin-singlet state is larger than in the spin-triplet one leading to a more attractive interaction in the spin-triplet partial wave due to a lower short-range repulsion. In fact, the hard cores caused by the color magnetic part of the OGE potential have been calculated obtaining 0.35 fm for the spin-triplet state and 0.44 fm for the spin-singlet one.

In conclusion is possible to note that the potential of  $\Lambda_c N$  system is less attractive with respect to other hyper-nucleus like  $\Lambda N$ , this fact could be explained from the following consideration.

- The long-range contribution is expected to be caused by the K meson exchange for  $\Lambda N$  interaction. In the system, however, the K meson (strange quark) exchange is replaced by the D meson (charm quark) exchange, and this contribution is highly suppressed due to the much heavier D meson mass than the K meson mass.
- The one-pion exchange in the  $\Lambda N - \Sigma N$  transition is considered to give a contribution to the effective  $\Lambda N$  interaction. Instead this contribution is expected to be suppressed due to the large mass difference between  $\Lambda_c N$  and  $\Sigma_c N$ .

### 4.0.3 Possible $\Lambda_c$ super-nuclei

One of the most interesting applications of the charmed baryon-nucleon interaction is the study of the possible existence of super-nuclei. A description of the potential had been taken from [30]. Since the  $\Lambda_c$  interaction is dominated by the spin-independent central force, as we discussed in the previous section, the spectrum of super-nuclei, if they exist, would probably can be approximated by the following single-folding potential defined by:

$$V_f(\vec{r}) = \int d^3r' \rho_A(\vec{r}') V_{\Lambda_c N}(\vec{r} - \vec{r}') \quad (4.12)$$

Where  $\rho_A(\vec{r})$  denotes the nuclear density distribution corresponding with the atomic number A and  $V_{\Lambda_c N}$  stands for the two body spin-independent central potential of the  $\Lambda_c$  system. The study described assumed,

$$\rho_A(\vec{r}) = \rho_0 \left[ 1 + e^{\frac{r-c}{a}} \right] \quad (4.13)$$

Where the parameters employed  $\rho_0$ , c, a are the same used for described spherical nuclei such as  $^{12}C$ ,  $^{28}Si$ ,  $^{40}Ca$ ,  $^{58}Ni$  and  $^{208}Pb$ . With the following potential they calculate the binding energy for  $\Lambda_c$  super-nuclei by the Gaussian expansion method for the S-wave potential. The result is shown in figure 4.5. As expected the binding energy increases with increasing atomic number. Furthermore varying the mass of the quark up and down in the simulation is observed that when their masses decrease toward physical values, and so the potential approach the physical one, the binding energy increases. These results suggest super-nuclei may exist, if their binding energy is larger than the Coulomb repulsion energy. For calculate the expectation value for the Coulomb potential energy they used a potential defined by.

$$V_C(\vec{r}) = \int d^3r' \rho_{ch}(\vec{r}') V_{Coulomb}(\vec{r} - \vec{r}') \quad (4.14)$$

Where  $V_{Coulomb}$  is an ordinary Coulomb potential and  $\rho_{ch}$  is charge density distribution obtained from elastic electron scattering for the previous nucleus. It's interesting to confront energy expectation taking into account also the Coulomb repulsion, the result is reported in figure 4.6. It's possible to see that for heavy nuclei the repulsion is too stench but for  $A = 12-58$  the expectation values of Coulomb force are not much stronger than the binding energy of  $\Lambda_c$  super-nuclei.

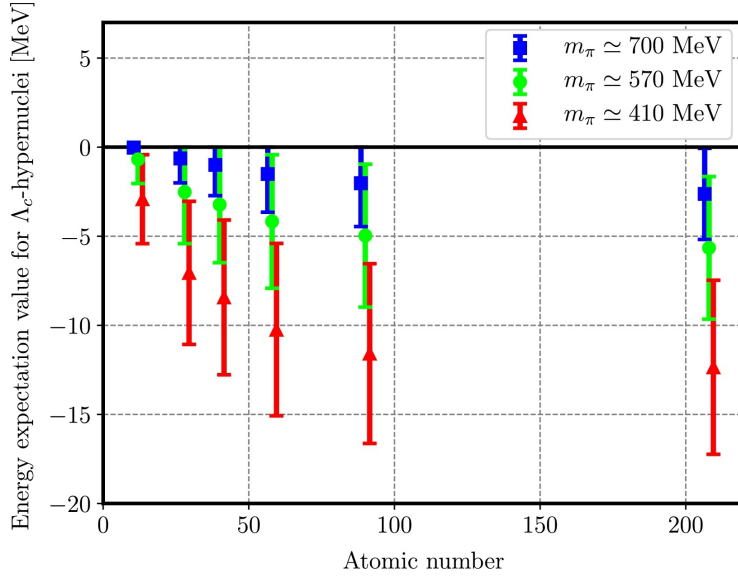


Figure 4.5: The figure show the binding energy in symmetric nuclei with the parameter assumed for each atomic number for each ensemble. The binding energies are calculated from the folding potentials for  $\Lambda_c$  super-nuclei by using the Gaussian expansion method. The folding potentials are constructed from the spin-independent central potential of the  $\Lambda_c$ N system

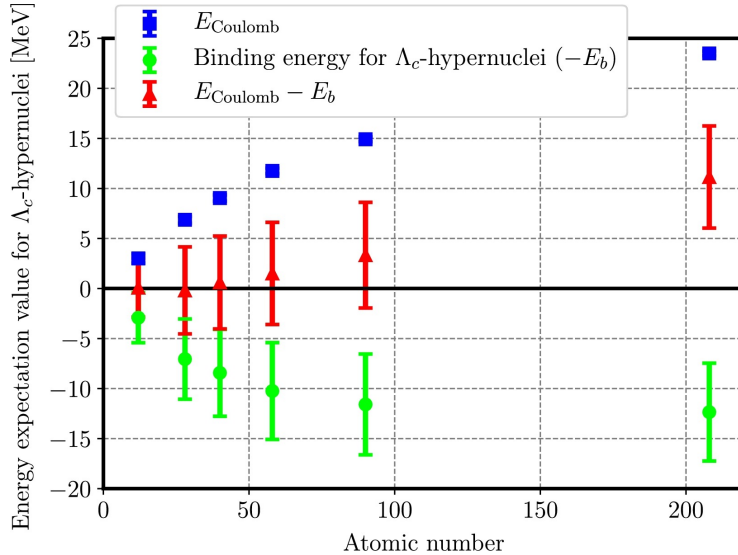


Figure 4.6: The figure show the expectation value of folding potential for Coulomb force in  $\Lambda_c$  super-nuclei (Blue). The expectation values are calculated from the binding solution of the  $\Lambda_c$  super-nuclei for Ensemble 3 ( $m_\pi \approx 410$  MeV). For comparison, the binding energy of  $\Lambda_c$  super-nuclei (Green) and sum of them (Red) are also plotted.

#### 4.0.4 C-deuteron ( $c - d$ ) simulation

Using an SHM model, we have tried to understand how the production of the super-nucleus is affected by various parameters. In particular, we focused on the c-deuteron, denoted  $c - d$  for convenience, which is a bound state of a  $\Lambda_c$  and a neutron. This choice is related to the fact that this nucleon is the easiest to observe in a heavy ion collision due to its mass. In fact, the lightest bound state of a  $\Lambda_c$  and a nucleus without Coulomb repulsion which makes the existence of this super-nucleus less likely. The first step was the super-nucleus characterization. The most probable configuration for its existence was chosen, i.e. the  $^3S_1$  state, so that the associated spin is  $1 \hbar$ . The mass was obtained by adding the mass of the  $\Lambda_c = 2286.46 \pm 0.14$  MeV/c $^2$  and the neutron mass  $m_n = 939.56542052(54)$  Mev/c $^2$  [31] removing then the binding energy. The latter value is still unknown, for this reason the binding energy of the deuteron was used,  $E_{be D} = (2.224575 \pm 0.000009)$  MeV [48], giving  $m_{c-d} \approx 3.223$  GeV/c $^2$ . One would expect a lower effective  $c - d$  binding energy, but as can be seen in 4.5, the order of magnitude is correctly individualized. Furthermore, since the binding energy is of the order of MeV/c $^2$  while the estimated mass is of the order of Gev/c $^2$ , the influence of this approximation can be neglected for the general evaluations made.

We then started the simulation using the Thermal FIST, for more information see [49], with a gran-canonical formalism based on Maxwell-Boltzmann statistics, thus neglecting quantum mechanical effects, for all particles except mesons, for which Bose-Einstein statistics were used due to their low mass. The focus was on central collisions, so a spherically symmetric shock wave momentum spectrum was assumed. For each combination of parameters,  $2 \cdot 10^7$  events were generated, setting the typical chemical potential observed in the LHC collision. The baryonic potential was  $\mu_B = 0.71$  MeV and the electric charge potential was  $\mu_Q = -0.18$  MeV as described in [4] for Pb-Pb collisions at  $\sqrt{s_{NN}} = 5.02$  Tev in ALICE<sup>1</sup>. Energy of the right order of magnitude for the temperatures analyzed. Instead, as described in [7], at the same energy in the center of mass the charm fugacity was  $\gamma_c = 29.6 \pm 5.2$ . However, this parameter was particularly important in determining the expected abundance of  $c - d$ , so it was changed in a second step. On the other hand, the chemical potential of strangeness had no influence on the following considerations, since no particle with a strange quark had been considered and was therefore considered to be zero. Dopo aver concluso la generazione si è ottenuto un istogramma che forniva il valore di  $dN/dy$  al variare di  $y$ , quindi per ottenere il valore complessivo per  $|y| < 0.5$  è stato effettuato l'integrale con numeri discreti. Per quanto riguarda le incertezze utilizzate per  $y$  si è scelto di associare una incertezza di mezzo bin che corrisponde a 0.006 mentre per quanto riguarda l'errore sul valore di  $dN/dy$  si è usata l'incertezza casuale fornita dal programma. The number of nucleus produced versus rapidity was

---

<sup>1</sup>The measured values were  $\mu_B = 0.71 \pm 0.45$  MeV while  $\mu_Q = -0.18 \pm 0.90$  MeV

then graphed for a chemical freeze-out temperature of 156 Mev and a radius of 8 fm in the range  $|y| < 0.5$ , obtaining the result shown in Fig ?? with the logarithmical scale on the y axis. Risulta in questo caso evidente come la massa il numero di particelle prodotte descresce esponenzialmente all'aumentare della massa e che si manifesta il fenomeno del "charm enhancement" visto che le abbondanze della  $\Lambda_c$  e del  $c - d$  sono superiori rispetto a quanto si attenderebbe per particelle con stessa massa ma senza la presenza del quark charm, come ben visibile dalle linee di fit. Inoltre i risultati della simulazione sono in accordo con quelli riportati in [alicecollaboration2022letterintentalice3]. La funzione su cui è stato eseguito il fit dei parametri era della forma  $y = ae^{bx}$ , dove a e b sono parametri liberi. Per i nuclei senza quark charm i valori ottenuti sono di  $a = (1.057 \pm 0.014) 10^4$  mentre  $b = (6.2107 \pm 0.0071) GeV^{-1}$  con un  $\tilde{\chi}^2 = 0.16$ . Il valore del  $\tilde{\chi}^2$  risulta essere particolarmente basso, ciò è dovuto anche al numero consistente di eventi generati che hanno diminuito l'incertezza statistica. Per quanto riguarda i nuclei con un quark charm sono  $a_c = (1.06904 \pm 0.017) 10^4$ , compatibile con il precedente valore, mentre  $b_c = (5.8730 \pm 0.0062) GeV^{-1}$ . Questi valori suggeriscono che potrebbe essere prodotto  $c - d$  a sufficienza per essere scoperto dai rivelatori di ALICE, anche se alcune delle problematiche che rendono complessa la sua individuazione verranno menzionate in seguito.

We then started to change the value of the temperature of chemical freeze-out and his radius. sono state analizzate delle temperature nel range fra 150 MeV a 160 con incrementi unitari per poter vedere come sarebbe cambiato localmente il numero di particelle prodotte fissando il raggio di freeze-out a 8 fm. Dai modelli statistici non era evidente quale sarebbe dovuto essere l'andamento osservato ma ci si aspettava un profilo esponenziale. Procedimento analogo è stato effettuato anche per il volume considerando raggi di freeze-out da 4 a 12 fm con incrementi unitari con una temperatura di freeze-out fissata a 156 MeV. Diversamente dal caso precedente il risultato atteso era prevedibile dall'Eq 3.25 quindi ci si aspettava un andamento  $N \propto r^3$  vista la simmetria sferica assunta. La figura 4.7 mostra gli effetti combinati di variazioni sui volumi e sulle temperature. Si riscontra che il numero di  $c - d$  attesi aumenta più rapidamente per incrementi del volume rispetto a quanto non si osservi per la temperatura. Bisogna però rimarcare come le variazioni percentuali sul raggio, e quindi sul volume, che sono state eseguite durante la simulazione risultano essere decisamente più consistenti rispetto a quanto non si sia fatto per le temperature. Analizzando con maggiore attenzione il risultato delle variazioni sul raggio visibile in Fig 4.8 si nota un andamento cubico perfettamente coerente con quanto previsto inizialmente ed un perfetto accordo visivo. La relazione con la quale è stato eseguito il fit era della forma  $ar^3 + b$  ed i risultati ottenuti sono stati  $a = (1.3921 \pm 0.0032) 10^{-6} fm^{-3}$  mentre  $b = (2.43 \pm 0.13) 10^{-8}$  con un  $\tilde{\chi}^2 = 0.42$ . Il valore del  $\tilde{\chi}^2$  suggerisce che la dipendenza funzionale è stata individuata correttamente.

Per quanto riguarda le valutazioni sugli incrementi di temperatura il risul-

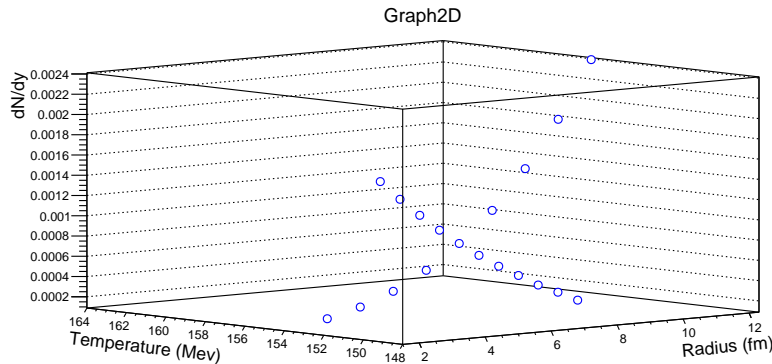


Figure 4.7: The figure shows the value of  $dN/dy$  of  $c - d$  in the range  $|y| < 0.5$  obtained from simulation by varying temperature and freeze-out radius. For variations in radius, temperature was fixed at 156 MeV while for variation in temperature, the radius was fixed at 8 fm.

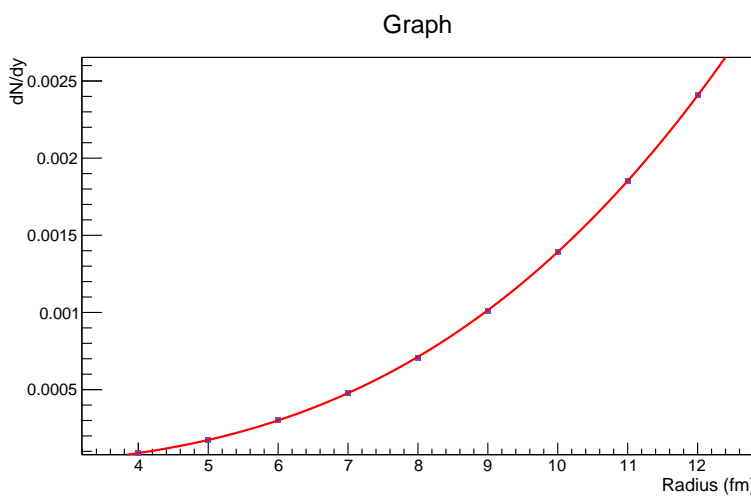


Figure 4.8: The figure shows the value of  $dN/dy$  of  $c - d$  in the range  $|y| < 0.5$  obtained from simulation by varying temperature and freeze-out radius. For variations in radius, temperature was fixed at 156 MeV while for variation in temperature, the radius was fixed at 8 fm.

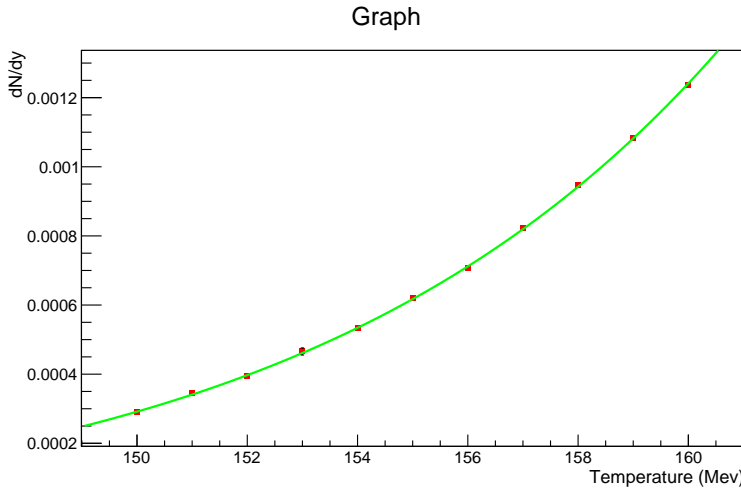


Figure 4.9: The figure shows the value of  $dN/dy$  of  $c - d$  in the range  $|y| < 0.5$  obtained from simulation al variare della temperatura e del raggio di freeze-out. Per le variazioni sul raggio la temperatura è stata fissata a 156 MeV mentre per la variazione sulla temperatura il raggio è stato fissato a 8 fm

tato è visibile in Figfig:var<sub>temperature</sub>. La relazione funzionale che meglio era capace di descrivere era  $e^{bT} + c$ , con  $a$ ,  $b$  e  $c$  parametri da determinare, il motivo di questo andamento non è chiaro e potrebbe essere solo un comportamento locale di una relazione funzionale più strutturata come la 3.13. I valori ottenuti sono stati di  $a = (1.19 \pm 0.17) 10^{-12}$ ,  $b = (0.13009 \pm 0.00087) MeV^{-1}$  e  $c = (-6.38 \pm 0.50) 10^{-6}$  con un  $\tilde{\chi}^2 = 1.05$ . L'ultimo valore suggerisce come nonostante non sia stato possibile procedere analiticamente partendo da Eq 3.25 comunque l'accordo con la relazione empirica risulta essere consistente. Questo risultato supporta inoltre quanto osservato in precedenza visto che gli aumenti in temperatura producono, almeno localmente, aumenti esponenziali quindi nonostante la Fig 4.7 possa suggerire che le variazioni nel raggio siano maggiormente impattanti ciò in realtà è legato alle variazioni percentuali maggiori seguite durante gli incrementi.

Si è poi cercato di capire come le variazioni nella charm fugacity influenzassero il risultato finale. Anche in questo caso è possibile fare una previsione analitica infatti partendo da Eq 3.25

$$\begin{aligned}
 \langle N \rangle &= \frac{\Delta V g_i}{2\pi^2 \hbar^3} \int_0^\infty dp \frac{p^2}{e^{-\beta(\mu_i - E)} + \theta_i} \\
 &\approx \frac{\Delta V g_i}{2\pi^2 \hbar^3} \int_0^\infty dp p^2 e^{\beta(\mu_i - E)} \\
 &= \frac{\Delta V g_i}{2\pi^2 \hbar^3} e^{\beta \mu_i} \int_0^\infty dp p^2 e^{-\beta E} \\
 &\propto \gamma_c
 \end{aligned} \tag{4.15}$$

We then analysed how its abundance varied with temperature and volume,

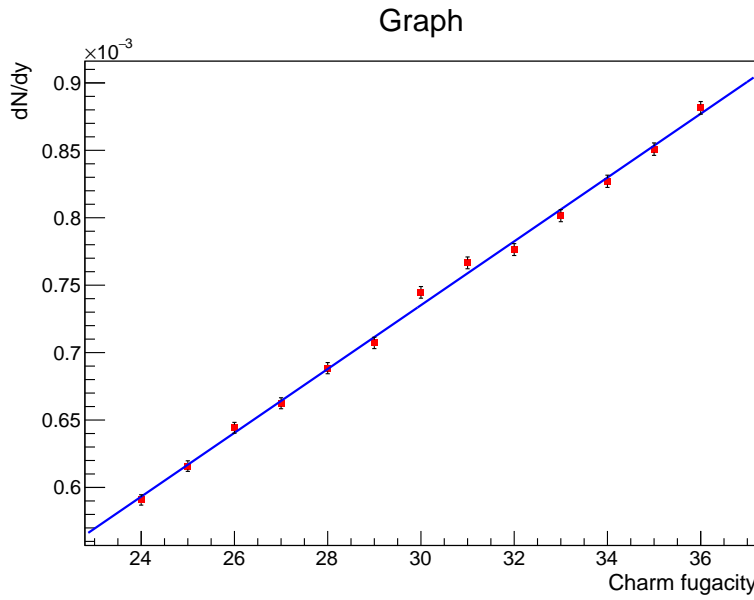


Figure 4.10: The figure shows the value of  $dN/dy$  of  $c - d$  in the range  $|y| < 0.5$  obtained from simulation al variare della temperatura e del raggio di freeze-out. Per le variazioni sul raggio la temperatura è stata fissata a 156 MeV mentre per la variazione sulla temperatura il raggio è stato fissato a 8 fm

obtaining the same results as shown in Figfig:comparison<sub>graph</sub>. Linear growth was found for increasing dimensional account can be seen in Eq??.

We have then moved analyze the detection of the

. Studying the data obtained from the previous simulations, an histogram to correlate the momenta of  $c-d$  with its occurrence was constructed. Then, using a Monte Carlo simulation with PYTHIA8, form factors were regenerated which had a distribution of moments based on what had been previously determined. A summary of the decay channels with their branching ratios is given in Eq??.

Quindi generando numeri casuali si è stimata la possibilità che i dueuteri vengano correttamente individuati. Il risultato finale è stato di



# Chapter 5

## ALICE

The A Large Ion Collider Experiment (ALICE) is a detector designed for heavy-ion physics at the Large Hadron Collider (LHC). It is primarily used to study lead-lead ( $^{208}\text{Pb}$ ) collision and so the most severe design constraint is to be able to withstand the high charge multiplicity expected for central events. During a collision conditions similar to those just after the Big Bang are recreated, condition that may also be present in neutron stars and other astrophysical objects. The ALICE collaboration uses the 10 000-tonne ALICE detector 26 m long, 16 m high, and 16 m wide. The detector sits in a vast cavern 56 m below ground close to the village of St Genis-Pouilly in France, receiving beams from the LHC. [50] The aim of ALICE is to recreate and study quark-gluon plasma, which is crucial for understanding the mechanisms that confine quarks and gluons, chiral symmetry restoration and the nature of the strong nuclear force. ALICE is currently the only experiment at the LHC specifically designed to study nuclear matter produced in relativistic heavy ion collisions and the QGP. For this reason, it must be able to measure as many observables as possible by studying all the different phenomena that can be attributed to the formation of a QGP state. It can estimate parameters such as the charged multiplicity of the interactions, the impact parameter, the shape and orientation of the fireball, the collision volume and the number of nucleons interacting in the collision. Almost all known Particle IDentification (PID) techniques are used in ALICE, such as: specific energy loss ( $dE/dx$ ), time-of-flight, Cherenkov radiation, electromagnetic calorimetry, muon detectors and topological reconstruction of decays. Despite all these identification techniques, it's very difficult to select signals of decays of heavy flavours, as will be explained in the last section, so the acquisition of a huge amount of data with a high efficiency of the data acquisition system (up to a frequency of 1.3 GB/s) is required.

A sketch of the ALICE coordinate system is shown in Fig 5.1 In this figure, the (x, y, z) axes are shown together with the cylindrical coordinates used to describe the trajectory of particles in ALICE,  $(r, \theta, \varphi)$ .

The ALICE sub-detectors are categorized into two main groups: one at

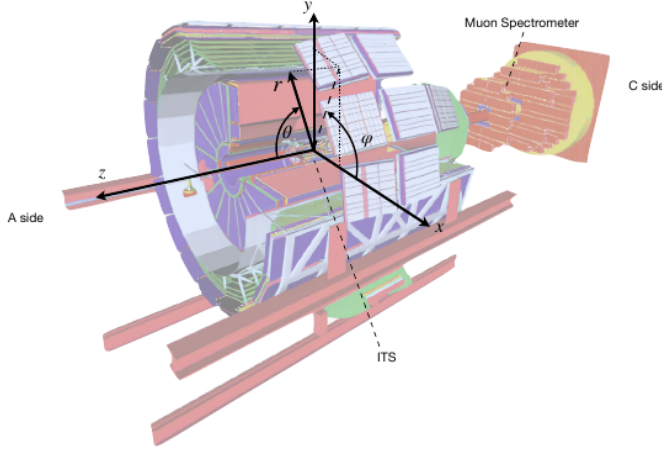


Figure 5.1: The figure show the cylindrical coordinate set used for describe the position of the object with respect the cartesian one [21].

mid-rapidity  $|\eta| < 1$ , the central barrel, and one at forward rapidity  $-4 < \eta < -2.5$ , that include also the muon spectrometer for muon identification. The apparatus scheme can be resumed in the following manner.

- The central barrel detectors can measure all over the azimuthal angle and are embedded in the L3 solenoid magnet, providing a maximum magnetic field strength of 0.5 T. It includes in order from the interaction point and going outward:

1. The **Inner Tracking System (ITS)** is a silicon tracking system composed of six cylindrical layers. Its main goal is to identify the position of the primary vertex with a resolution better than  $100 \mu\text{m}$  and provide tracking of charged particles.
2. the **Time Projection Chamber (TPC)** is used for charged particle identification.
3. the **Transition Radiation Detector (TRD)** is composed of different gas chamber and radiation for identify and track electrons
4. the **Time of Flight (TOF)** measure the time of flight providing important information for particle identification. It can also provide a trigger specific for cosmic ray events and Ultra Peripheral Collision collisions (UPC).

These subsystem are mostly dedicated to vertex reconstruction, tracking, particle identification and momentum measurement. Are also present some specialized detectors with limited acceptance.

1. **High-Momentum Particle Identification Detector (HMPID)** is used for study Cherenkov photons for identify particle with  $p_{\perp} > 1 \text{ GeV}/c$

2. **PHOton Spectrometer (PHOS)** is an electromagnetic calorimeter used for photons identification and as high-energy photon trigger.
  3. **ElectroMagnetic CaLorimeter (EMCal)** is a Pb-scintillator calorimeter for identify photons and pion with  $\eta > 0.7$  and is also used as jet trigger.
  4. **Di-jet Calorimeter (DCal).**
- The forward detector include:
    1. **Muon spectrometer** for reconstruct heavy quark hadrons thought their weak decay in the channel  $\mu^-\bar{\nu}_\mu$  or  $\mu^+\nu_\mu$  or for electrodynamic decay in the couple  $\mu^+\mu^-$
    2. **Forward Multiplicity Detector (FMD)** composed by several layers of silicon strip detectors at a distance of  $70 \div 150$  cm from the interaction point.
    3. **Photon Multiplicity Detector (PMD)**
    4. **Zero Degree Calorimeters (ZDC)** a proton and neutron calorimeter
    5. **V0 Detectors**
    6. **T0 detectors**

[34] [8]

In the following section we will discuss some of the most important one.  
A graphical resume is visible in Fig 5.2

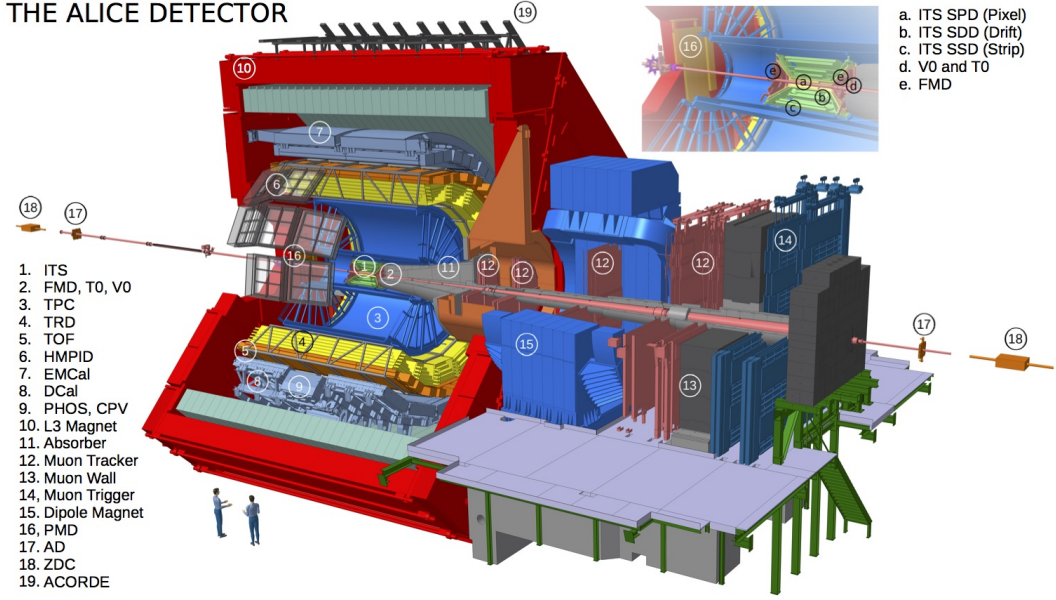


Figure 5.2: The figure show the Layout of the ALICE detector in Run2 with their position and dimension [12]

### 5.0.1 Inner Tracking System (ITS)

The Inner Tracking System (ITS) is a crucial part of the ALICE tracking system, positioned as the innermost sub-detector of the central barrel, closest to the beam pipe and the interaction point. It consists of six concentric cylindrical layers of silicon detectors, comprising two layers each of Silicon Pixel Detector (SPD), Silicon Drift Detector (SDD), and Silicon Strip Detector (SSD). The ITS covers the pseudorapidity region  $|\eta| < 0.9$  for interactions occurring within 10 cm from the detector point. The SPD is located at radial

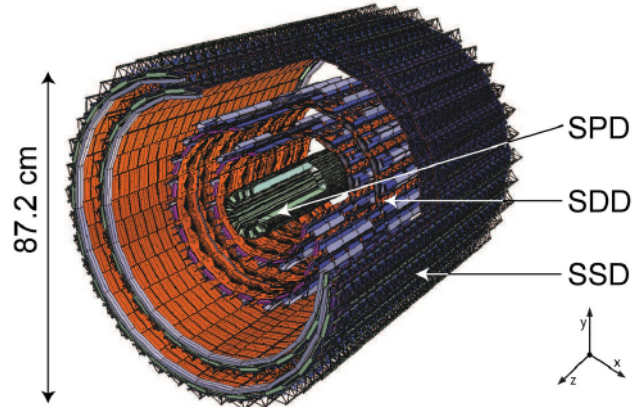


Figure 5.3: Schematic diagram of the Inner Tracking System (ITS) of the ALICE experiment [15]

distances of 3.9 cm and 7.6 cm from the beam pipe. These layers cover extended pseudorapidity ranges of  $|\eta| < 2.0$  and  $|\eta| < 1.4$ , respectively. They consist of hybrid silicon pixel detectors, in total  $9.8 \cdot 10^6$ , which generate binary signals when traversed by charged particles, facilitating their counting. The primary functions of the SPD are to determine the position of the primary vertex with a high resolution, surpassing  $100 \mu\text{m}$ , to help isolate events coming from pileup, and to contribute to the triggering system due to their fast response. The SPD also contributes to achieving an impact-parameter resolution surpassing  $50 \mu\text{m}$  for tracks with transverse momentum  $p_\perp > 1.3 \text{ GeV}/c$ . The two intermediate layers are the SDD, situated at radii of 15.0 cm and 23.9 cm, covering  $|\eta| < 0.9$ . The SDD has very good multi-track capability and provides two out of the four measurements of specific  $dE/dx$  employed for PID by the ITS. It provides two-dimensional spatial information ( $r \phi$  and  $z$ ) with a spatial resolution of  $35 \mu\text{m}$  ( $r \phi$ ) and  $25 \mu\text{m}$  ( $z$ ). The SDD determines particle positions using drift time estimation and charge centroid measurement for these reason is structured with a central cathode for more precise particle tracking. The two outermost layers employ double-sided Silicon Strip Detectors (SSD), located at radial distances of 38.0 cm and 43.0 cm, covering  $|\eta| < 1.0$ . The SSD is essential for the prolongation of tracks from the main tracking detector of ALICE, the Time Projection Chamber (TPC), to the ITS. It provides a spatial resolution of  $20 \mu\text{m}$  ( $r \phi$ ) and  $830 \mu\text{m}$  ( $z$ ) and  $27 \mu\text{m}$  ( $r \phi$ ) and  $830 \mu\text{m}$  ( $z$ ), with a readout time of  $1 \mu\text{s}$ . Besides connecting tracks, the SSD also provides  $dE/dx$  information. The ITS can also perform "standalone" tracking for charged particles in the low  $p_\perp$  region by using exclusively the information from its six layers. [34] [22] [14] [8]

### 5.0.2 Time projection chamber (TPC)

The Time projection chamber is the main tracking detector of the central barrel. It is specifically designed for measure tracks with transverse momentum range  $0.1 - 100 \text{ Gev}/c$  and pseudorapidity range  $|\eta| < 0.9$ . It is positioned at radial distances ranging from 85 to 247 cm from the beam pipe, extending along the beam direction with a total length of 510 cm. It is divided along the beam axis into two equally large drift regions by a central cathode, each having a length of 2.5 m. On the opposite sides of the central electrodes there is the readout plate, which is equipped with multi-wire proportional chambers (MWPC). Each of the 18 readout chambers covers an azimuth of  $20^\circ$ . The volume of the TPC ( $\sim 90 \text{ m}^3$ ) can be filled with different gases depending on the running conditions. A graphical resume is visible in Fig 5.4 The perfect candidate is a gas with a small radiation length and low multiple scattering rates, so is usually filled with a mixture containing various combinations of argon, neon, carbon dioxide and sometimes nitrogen. When charged particles pass through the gas, they ionize it, creating an electron-ion pair. These ionization electrons then drift towards sensing electrodes under a uniform electric

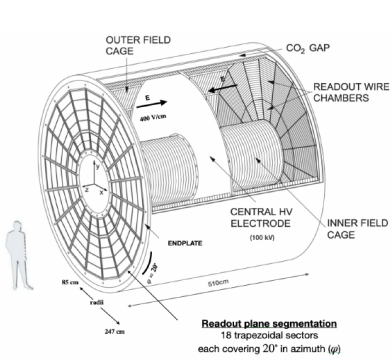


Figure 5.4: The figure show a schematic representation of the time projection chamber [17]

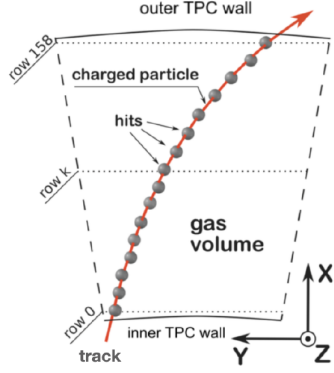


Figure 5.5: The figure show a diagram of the TPC tracking method [37]

field, typically achieved by applying a high voltage of around 100 kV between the central electrode and the readout plates. The ionization electrons drift with a speed of approximately 2.7 cm/s, corresponding to a maximum drift time of around 92 ms. This drift process allows spatial localization of the ionization event along the particle trajectory. In addition, the presence of a uniform magnetic field along the z-direction causes charged particles to bend into curved trajectories. This allows precise momentum measurements. The position resolution for the inner/outer radii ranges from 800 to 1100  $\mu\text{m}$  in the transverse plane ( $r \phi$ ) and from 1100 to 1250  $\mu\text{m}$  along the beam axis ( $z$ ). The total charge collected at the end plates for each track is proportional to the particle energy loss in the gas. This allows a sampling of the  $dE/dx$  and therefore perform PID below 1 GeV/c. The resolution on the  $dE/dx$  is 5% for isolated tracks (low multiplicity collisions), while when the number of particles increase such as Pb–Pb collisions (high multiplicity collisions), the resolution is 7%. This is due to the increased probability to have hits close in space. In addition, the contribution of positive ions to the signal shape increases with the particle occupancy and the formation of large amount of charged particles can induce local modifications to the external electric field modifying the drift speed and complicating the reconstruction of the track. The specific energy loss can be described by the Bethe-Bloch formula, which depends on the particle species, its momentum, and the properties of the traversed medium. It can be estimated in the following manner proposed by [38].

$$f(\beta) = \frac{P_1}{\beta^{P_4}} \left( P_2 - \beta^{P_4} - \ln(P_3) \frac{1}{(\beta\gamma)^{P_5}} \right) \quad (5.1)$$

Where  $\beta$  is the particle velocity in c unit,  $\gamma$  the Lorentz factor,  $P_{1-5}$  free parameter that must be estimated from data.

[34] [22] [14] [8]

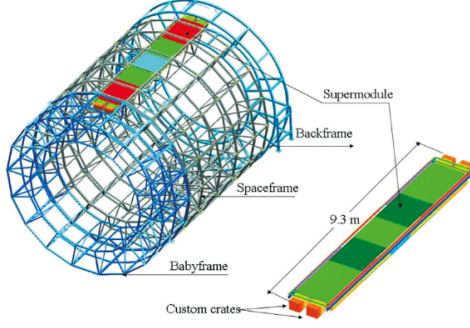


Figure 5.6: The figures show the structures of the time of flight detector [3].

### 5.0.3 Time Of Flight (TOF)

The Time Of Flight (TOF) detector is a large array of Multi-gap Resistive-Plate Chambers (MRPC), located at 3.7 m and 3.99 m radial distance, respectively, from the interaction point. It is designed to identify charged particle produced in pseudorapidity of  $|\eta| < 0.9$  and with an intermediate momentum range ( $0.5 < p_{\perp} < 4$  GeV/c). In addition TOF has been used to provide a trigger specific for cosmic ray and Ultra Peripheral Collision UPC events. The TOF detector has a modular structure divided along the azimuthal direction into 18 super modules as visible in Fig 5.6. If a particle ionizes the gas in the detector, an avalanche process will be triggered to generate signal on the readout electrodes. Particle identification is performed by combining the information bring by the linear momentum module ( $p$ ) and track length ( $l$ ) with the measurement of the time of flight ( $t$ ) in TOF. The mass ( $m$ ) corresponding to the one of the detected particle can be obtained.

$$p = m\gamma\beta c \longleftrightarrow m = \frac{p\sqrt{1 - \beta^2}}{c\beta} = \frac{p\sqrt{\frac{1}{\beta^2} - 1}}{c} \quad (5.2)$$

The  $\beta$  parameter can be measured in the following manner

$$\beta = \frac{v}{c} = \frac{l}{c t} \quad (5.3)$$

So

$$m = \frac{p\sqrt{\left(\frac{t}{lc}\right)^2 - 1}}{c} \quad (5.4)$$

Studying the equation became clear that, at large momenta, the resolution on the track momentum ( $\sigma_p$ ) becomes negligible and the total uncertainty is driven by the uncertainties on the timing ( $\sigma_t$ ) and track length ( $\sigma_l$ ). For these reason the TOF detector was designed to achieve a timing resolution better than 40 ps with a detector efficiency close to 100%. [34] [22] [14]

### Transition Radiation Detector (TRD)

The Transition Radiation Detector (TRD) is positioned between the TPC and TOF detector and it covers a pseudorapidity range of  $|\eta| < 0.84$ . It is principally used for electron identification in high momentum region ( $p > 1$  GeV), where discriminating between electrons and pions using traditional  $dE/dx$  techniques becomes challenging. When charged particles attempt to cross the detector, pass through two media with different dielectric constants emitting so transition radiation with an intensity proportional to their Lorentz factor. Since different particles have different masses and velocities, they emit different amounts of transition radiation making the identification possible. [34] [22]

### Photon Spectrometer (PHOS)

The Photon Spectrometer (PHOS) it's an electromagnetic calorimeter known for its high spatial and energy resolution thanks to a scintillating material called Lead Tungstate ( $PbWO_4$ ). It covers a pseudo-rapidity range of  $|\eta| < 0.12$  with a dynamic energy range from 0.1 GeV to 100 GeV. Its main goal is to measure QGP temperature, space-time dimensions and study deconfinement through jet quenching. [34] [22]

### High-Momentum Particle Identification Detector (HMPID)

The High Momentum Particle Identification Detector (HMPID) is dedicated to the identification of charged hadrons with  $p_T > 1$  GeV/c, thus extending the PID capabilities of the ITS, TPC and TOF at high momentum. It covers a pseudorapidity range of  $-0.6 < \eta < 0.6$  and consists mainly of two parts: the radiator and the photon detector composed by seven Ring Imaging Cherenkov (RICH) counters. [34] [22]

### Electromagnetic Calorimeter (EMCal)

The EMCal consists of towers of  $6 \times 6 \times 20$  cm<sup>3</sup> each, made up of 76 alternating layers of lead and scintillator (not uniform, unlike PHOS). It was designed to measure electrons from the decay of heavy flavour hadrons, but not only. It also identifies high-energy particles and enhances energy resolution across various momenta, enabling precise measurements of jet quenching, high-energy jets, and high-momentum electrons and photons. [34] [8]

#### 5.0.4 Forward Detectors

##### VZERO detector (V0)

The V0 detector consists of two circular arrays of scintillator counters (named V0A and V0C) one per side with asymmetric distance from the interaction

point. The V0A covers the pseudorapidity region  $2.8 < \eta < 5.1$  while V0C  $-3.7 < \eta < -1.7$ . They are important both in pp collision and AA collision for the following reason;

- **Triggering:** The V0 detector provides a minimum bias trigger signal. This is important because help to detect a broad range of inelastic collision events without introducing significant selection bias.
- **Rejection background events:** The VZERO detector help in the rejection of background events generated due to the interaction of beams with residual gas within the beam pipe and with mechanical structures. This is possible thanks to the time gap between signals from V0A and V0C.
- **Centrality determination:** The signal given by the V0 detector is proportional to the number of particles traversing it furnishing information about the multiplicity and centrality of the collision. This data are precious for understanding the collision geometry and interpreting experimental results accurately.

[34] [22]

## T0 Detectors

The T0 detector consists of two arrays, T0A and T0C, of Cherenkov counters placed along the beam pipe on each side of the interaction point, respectively at -72.7 cm and 375 cm. The pseudorapidity coverage are  $4.61 < \eta < 4.92$  (T0A) and  $-3.28 < \eta < -2.97$  (T0C). Its primary function is to provide a fast timing signal for the TOF detector, serving as a collision time reference. It can be also use for an independent determination of the vertex position along the beam axis (with a precision of  $\pm 1.5$  cm). [34] [22]

## Zero Degree Calorimeter (ZDC)

The Zero Degree Calorimeter (ZDC) consists of four calorimeters, two for protons (brass-quartz proton ZP) and two for neutrons (tungsten-quartz neutron ZN), on each side. located at  $\sim 112.5$  cm away from the interaction point, symmetrically in both directions. The ZDC measures the energy of the spectator nucleons and assists in the estimation of centrality and luminosity in heavy ion collisions by determining the collision geometry, overlap regions of the colliding nuclei and the number of participating nucleons.[34] [22]

## Muon Spectrometer

The muon spectrometer is located 14 m in the negative beam direction and cover a pseudorapidity range of  $4 < \eta < 2.5$ . It help to studies the complete

spectrum of heavy quarkonia via their decay in the  $\mu^+\mu^-$  channel. It is composed of different part. The particles cross first an absorber, mainly composed of carbon and concrete, designed to absorb the hadrons emerging from the interaction point. This material choice is for limit the multiple scattering and the energy loss of the muons. The muons then traverse five tracking stations and are deflected by the magnetic field allowing for the determination of their momentum. The dipole magnet provide a magnetic field nominally of  $B = 0.7$  T but can be changed by the requirements on the mass resolution. The next part is the muon filter, an iron wall designed to reduce the background in the trigger chambers by absorbing secondary hadrons and low momentum muons. Finally, the muons reach the trigger system, which consists of two stations equipped with resistive plate chambers characterized by a time resolution of about 1 ns. [34] [51] [21]

### 5.0.5 Track and vertex reconstruction

To reconstruct particle's trajectory a tracking algorithms is used [14]. This process employ the Kalman filter algorithm, which use the information contained in a data cluster and transforms them into tracking information to obtain the best possible approximation of the real trajectory. It is implemented in a three-pass tracking scheme known as inward-outward-inward.

The tracking procedure starts with the clustering step performed separately by each detector in witch, starting from the raw data, clusters are created. The clusters are groups of hits produced by a single particle interaction with a detector element and contain its positions, signal amplitudes, signal times and their associated errors. Then the first inward stage starts. As a first step, the track seeds are built from the clusters of the two outermost pad rows of the TPC and the primary vertex point as a constraint. For determine the interaction vertex the information provided by the SPD detector plays a crucial role because is closest to the interaction point, and has excellent transverse plane resolution due to its high granularity. The resolution of the SPD Vertex is of  $10 \mu\text{m}$  in Pb–Pb collisions and  $150 \mu\text{m}$  in pp collisions at  $\sqrt{s_{NN}} = 7 \text{ TeV}$ . For find the vertex position the algorithm search the space point that minimises the distance among the tracklets, which are the track segments reconstructed by associating pairs of clusters in the two SPD layers, localizing the point where most of the tracklets converge. When pileup interaction is expected, like in the hight multiplicity events, the algorithm is repeated several times, discarding at each iteration those clusters which contributed to already-found vertices. When the primary vertex has been localize the algorithm start to search the tracklets that fulfill certain proximity cuts trying to reconstruct the path from the interaction vertex and the data of the TPC. Sometimes happen that the same physical track is reconstruct multiple times; to mitigate this issue, a dedicated algorithm is used to identify pairs of tracks that share a fraction of common clusters above a

certain threshold, typically ranging from 25% to 50%. The efficiency of the track reconstruction process is influenced by the transverse momentum of the tracks and drops below  $p_{\perp} < 0.5$  GeV/c, as visible in Fig 5.9 due to energy loss in the detector material, while for higher  $p_{\perp}$  the efficiency is affected by the path followed, as it may pass through areas where clusters are lost due to dead zones between read sectors. [34]. In the second step the track reconstructed thanks to the TPC are used as seed for the propagation of the outer track. As these seeds are propagated inward, they are continuously updated by incorporating clusters within a defined proximity cut. In this way a tree of track hypothesis is created using the new seed generated by each update. The final candidates tracks are selected based on their  $\tilde{\chi}^2$  penalizing the case in which cluster are not found during the extrapolation except for the passage in the dead zones of the detector. In the last stage, the reconstructed tracks are propagated starting from the outer TPC radius toward the interaction point for refine the track parameter. Finally the Kalman filter provides the track parameters including: position, direction, and inverse curvature, with the associated covariance matrix.

For the study of the heavy-flavor sector the Muon Forward Tracker (MFT) plays a crucial role. The MFT has been designed to allow a clean identification of prompt/displaced muon sources, resulting in particular in the possibility of having charm/beauty separation and background reduction in the light-flavor sector. The MFT tracking algorithm can be separated into two steps: the track finding and the track fitting. For the track finding two methods are used. The first one is called Linear Track Finder (LTF) that looks for cluster position aligned along a straight line although the magnetic field curve the trajectory of charged particle, but the deviation can be neglected at least at high  $p_{\perp}$ . For help in these work a radial tolerance  $R_{\text{cut}}$  is given, a graphical resume is visible in Fig 5.7. If a track had been recognized in the previous step the correspondent clusters are removed from the list of available ones and are not more considered. The next step consist on a Cellular Automaton (CA) approach particularly suited for low-momentum tracks. It is based on a propagation and joining of consecutive tracklets. So starting from a given segment, considered as the first, the algorithm search the further ones imposing track continuity conditions. The strategist is visible in Fig 5.8. Only after that the track candidates are found a track fitting algorithm is applied in order to extract the kinematic parameters. It is able to determine the spatial and momentum coordinates considering material effects. [21].

Once the tracks and the interaction vertex have been found a search for photon conversions and secondary vertices from particle decays is performed. In ALICE, secondary vertex reconstruction begins by selecting tracks with Distance of Closest Approach DCA greater than 0.5 mm in pp collisions or 1 mm in Pb–Pb collisions. A graphical resume is visible in Fig ???. For each pair of selected tracks with opposite charges, known as  $V^0$  candidates, are then subjected to further selection criteria:



Figure 5.7: The figure show Linear Figure 5.8: The figure show how the Track Finder schematic using the Cellular Automaton method works [46]  
RCut parameter [46]

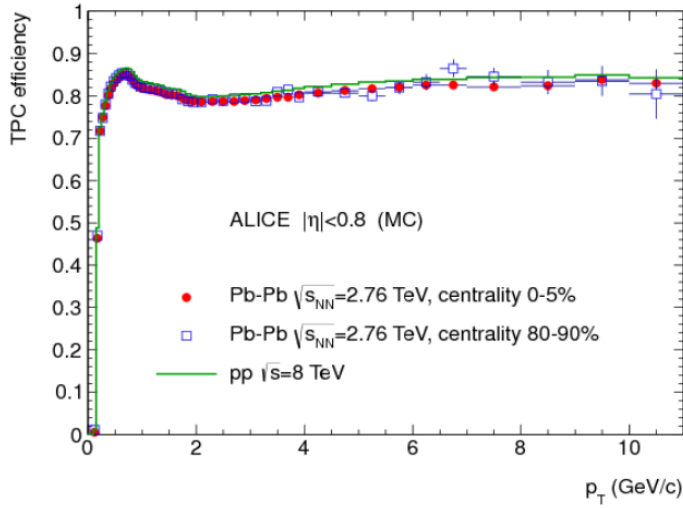


Figure 5.9: The figure show track finding efficiency for primary particles in different types of collision [3]

1. The distance between the two tracks at their PCA is requested to be less than 1.5 cm
2. The PCA is requested to be closer to the interaction vertex than the innermost hit of either of the two tracks.
3. The cosine of the angle between the total momentum vector of the pair and the line connecting the primary and secondary vertices must be greater than 0.9

For  $V^0$  candidates with a momentum below 1.5 GeV/c the cut are relaxed. For the study of heavy-flavor decays close to the interaction point, the secondary vertex is searched starting from point that satisfied other different topological condition. [3] The secondary vertex are then reconstructed with the same algorithm used to compute the primary vertex from tracks. The resolution on the position of secondary vertex can be estimated by Monte Carlo simulations to be of the order of 100  $\mu\text{m}$  with little  $p_T$ -dependence for  $p_T > 1 \text{ GeV}/c$  [2]. For this reason it is particularly difficult to detect particles with charm flavour,

because for example the  $\Lambda_c$  has a mean life of  $t = (2.024 \pm 0.031) 10^{-13}$  s, so it can move away from the interaction point for  $ct \approx 60 \mu\text{m}$ , less than the instrument resolution. For this reason it is impossible to clearly distinguish the two vertices, making the analysis much more complex.



# Chapter 6

## Appendix

### A Appendix A

Starting with the proof that  $dyp_{\perp}dp_{\perp}d\phi_p = dy m_{\perp}dm_{\perp}d\phi_p$ , in fact  $m_{\perp} = \sqrt{m^2 + p_{\perp}^2}$  so  $\frac{dm_{\perp}}{dp_{\perp}} = \frac{p_{\perp}}{\sqrt{m^2 + p_{\perp}^2}} = \frac{p_{\perp}}{m_{\perp}}$  and the result follow immediately.

For the other equation starting from 3.8 and inserting 3.2 one get

$$\begin{aligned} \frac{dN_i}{dy m_{\perp} dm_{\perp} d\phi_p} &= \frac{g_i}{(2\pi)^3} \sum_{n=1}^{\infty} (\pm)^n \int d^2 r_{\perp} \tau_f e^{n\mu_i/T} e^{n\gamma_{\perp} v_{\perp} \cdot p_{\perp}} \\ &\quad \int_{-\infty}^{+\infty} d\eta (m_{\perp} \cosh(y - \eta) - \vec{p}_{\perp} \cdot \nabla_{\perp} \tau_f) e^{-n\gamma_{\perp} m_{\perp} \cosh(y - \eta)/T} \\ &= \frac{g_i}{(2\pi)^3} \sum_{n=1}^{\infty} (\pm)^n \int d^2 r_{\perp} \tau_f e^{n\mu_i/T} e^{n\gamma_{\perp} v_{\perp} \cdot p_{\perp}} \\ &\quad \left( m_{\perp} K_1 \left( nm_{\perp} \frac{\gamma_{\perp}(\vec{r}_{\perp})}{T(\vec{r}_{\perp})} \right) - \vec{p}_{\perp} \cdot \nabla_{\perp} \tau_f K_0 \left( nm_{\perp} \frac{\gamma_{\perp}(\vec{r}_{\perp})}{T(\vec{r}_{\perp})} \right) \right) \end{aligned} \quad (1)$$

Where the modified Bessel function enters the game. The azimuthal integral can thus be done analytically

$$\begin{aligned} \frac{dN_i}{dy m_{\perp} dm_{\perp}} &= \frac{g_i}{\pi^2} \sum_{n=1}^{\infty} (\pm)^n \int_0^{\infty} r_{\perp} dr_{\perp} \tau_f e^{n\mu_i/T} \\ &\quad \left( m_{\perp} K_1 \left( nm_{\perp} \frac{\gamma_{\perp}(\vec{r}_{\perp})}{T(\vec{r}_{\perp})} \right) I_0 \left( n \frac{p_{\perp} v_{\perp} \gamma_{\perp}}{T} \right) \right. \\ &\quad \left. - p_{\perp} \frac{\partial \tau_f}{\partial r_{\perp}} K_0 \left( nm_{\perp} \frac{\gamma_{\perp}(\vec{r}_{\perp})}{T(\vec{r}_{\perp})} \right) I_1 \left( n \frac{p_{\perp} v_{\perp} \gamma_{\perp}}{T} \right) \right) \end{aligned} \quad (2)$$

And finally, defining  $v_{\perp} = \tanh(\rho)$  and  $\eta(\vec{r}_{\perp}) = \tau_f e^{n\mu_i/T}$ , one obtains

$$\frac{dN_i}{dy m_\perp dm_\perp d\phi_p} = \frac{g_i}{\pi} \int_0^\infty r_\perp dr_\perp n_i(r_\perp) \left[ m_\perp K_1 \left( \frac{m_\perp \cosh(\rho(r_\perp))}{T(r_\perp)} \right) I_0 \left( \frac{p_\perp \sinh(\rho(r_\perp))}{T(r_\perp)} \right) - p_\perp \frac{\partial \tau_f}{\partial r_\perp} K_0 \left( \frac{m_\perp \cosh(\rho(r_\perp))}{T(r_\perp)} \right) I_1 \left( \frac{p_\perp \sinh(\rho(r_\perp))}{T(r_\perp)} \right) \right] \quad (3)$$

## B Appendix B

Under free-streaming the phase space distribution evolves as

$$f(\vec{r}, \vec{p}, t) = f(\vec{r} - \frac{\vec{p}}{E}(t - t_0), \vec{p}, t) \quad (4)$$

Using a Gaussian parametrization for the initial phase-space distribution of produced secondary particles

$$f(\vec{r}, \vec{p}, \tau) = e^{-\frac{x^2}{2R_x^2} - \frac{y^2}{2R_y^2} - \frac{p_x^2 + p_y^2}{2(\Delta\tau)^2}} \quad (5)$$

where  $\Delta t$  so writing the Eq 3.17 in integral form.

$$\epsilon_x = \frac{\int d^2r r^2 \cos(2\psi_r \int d^3p f(\vec{r}, \vec{p}, \tau))}{\int d^2r r^2 \int d^3p f(\vec{r}, \vec{p}, \tau)} \approx \frac{R_x^2 + R_y^2}{R_x^2 + R_y^2 + 2(c\Delta\tau)^2} \quad (6)$$

One get

$$\frac{\epsilon_x(t_0 + \Delta T)}{\epsilon_x(\tau_0)} = \left[ 1 + \frac{(c\Delta\tau)^2}{\langle \vec{r}^2 \rangle_{\tau_0}} \right]^{-1} \quad (7)$$

## C Appendix C

For get the gran canonical partition function starting from Eq 3.24 visible below.

$$\ln Z_i(T, V, \mu_i) = \frac{\Delta V g_i}{2\pi^2 \hbar^3} \int_0^\infty \theta_i p^2 dp \ln(1 + \theta_i e^{\beta(\mu_i - E)}) \quad (8)$$

replacing the logarithm with taylor expansion under the assumption that  $e^{\beta(\mu_i - E)} < 1 \rightarrow \mu_i < E$  and using  $\lambda_i = e^{\beta\mu_i}$  it's possible to rewrite 3.2.

$$\ln Z_i(T, V, \mu_i) = \frac{\Delta V g_i}{2\pi^2 \hbar^3} \sum_K \frac{(\theta\lambda_i)^k}{k} \int_0^\infty p^2 dp e^{-k\beta E} \quad (9)$$

integrating by part

$$\ln Z_i(T, V, \mu_i) = \frac{\Delta V g_i}{2\pi^2 \hbar^3} \sum_K \frac{(\theta\lambda_i)^k}{k} \left[ \frac{p^3 e^{-k\beta E}}{3} \Big|_0^\infty + \int_0^\infty dp \frac{p^3 k \beta e^{-k\beta E}}{3} \frac{dE}{dp} \right] \quad (10)$$

The first integrand vanish.

$$\frac{dE}{dp} = \frac{d}{dp}(\sqrt{p^2 + m_i^2}) = \frac{p}{\sqrt{p^2 + m_i^2}} = \frac{p}{E} \quad (11)$$

so

$$\ln Z_i(T, V, \mu_i) = \frac{\Delta V g_i}{2\pi^2 \hbar^3} \sum_K \frac{(\theta \lambda_i)^k}{k} \int_0^\infty dp \frac{p^3}{3} \frac{k \beta e^{-k\beta E}}{p} \frac{E}{p} \quad (12)$$

introducing  $x = k\beta E$ ,  $w_i = k\beta m_i$  and  $y_i = x/w_i$

$$\ln Z_i(T, V, \mu_i) = \frac{\Delta V g_i}{2\pi^2 \hbar^3} \sum_K \frac{(\theta \lambda_i)^k}{k} \int_0^\infty dE \frac{p^3 k \beta e^{-k\beta}}{3} \quad (13)$$

$$\ln Z_i(T, V, \mu_i) = \frac{\Delta V g_i}{2\pi^2 \hbar^3} \sum_K \frac{(\theta \lambda_i)^k}{k} \int_0^\infty dE \frac{(E^2 - m_i^2)^{3/2} k \beta e^{-k\beta}}{3} \quad (14)$$

$$\ln Z_i(T, V, \mu_i) = \frac{\Delta V g_i m_i^2}{2\pi^2 \hbar^3 \beta} \sum_K \frac{(\theta \lambda_i)^k}{k^2} \int_0^\infty dE \frac{(x^2 - w_i^2)^{3/2}}{3w_i^2} e^{-x} \quad (15)$$

$$\ln Z_i(T, V, \mu_i) = \frac{\Delta V g_i m_i^2}{6\pi^2 \hbar^3 \beta} \sum_K \frac{(\theta \lambda_i)^k w_i}{k^2} \int_0^\infty dE \left( \frac{x^2}{w_i^2} - 1 \right)^{3/2} e^{-x} \quad (16)$$

$$\ln Z_i(T, V, \mu_i) = \frac{\Delta V g_i m_i^2}{6\pi^2 \hbar^3 \beta} \sum_K \frac{(\theta \lambda_i)^k w_i}{k^2} \int_0^\infty dE w_i (y^2 - 1)^{3/2} e^{-w_i y} \quad (17)$$

introducing the modified Bessel function

$$k_2(q) = \frac{q^2}{3} \int_0^\infty dy (y^2 - 1)^{3/2} e^{-qy} \quad (18)$$

and finally

$$\ln Z_i(T, V, \mu_i) = \frac{\Delta V g_i}{2\pi^2 \hbar^3 \beta} \sum_K \frac{(\theta_i e^{\beta \mu_i})^k}{k^2} m_i^2 K_2(k\beta m_i) \quad (19)$$



# Bibliography

- [1] "Mattia". *Evolution of collisions and QGP*. URL: <https://particlesandfriends.wordpress.com/2016/10/14/evolution-of-collisions-and-qgp/#respond>.
- [2] B. Abelev et al. "Measurement of charm production at central rapidity in proton-proton collisions at  $\sqrt{s} = 2.76$  TeV". In: *Journal of High Energy Physics* 2012.7 (July 2012). ISSN: 1029-8479. DOI: 10.1007/jhep07(2012)191. URL: [http://dx.doi.org/10.1007/JHEP07\(2012\)191](http://dx.doi.org/10.1007/JHEP07(2012)191).
- [3] Betty Bezverkhny Abelev et al. "Performance of the ALICE Experiment at the CERN LHC". In: *Int. J. Mod. Phys. A* 29 (2014), p. 1430044. DOI: 10.1142/S0217751X14300440. arXiv: 1402.4476 [nucl-ex].
- [4] S. Acharya et al. "Measurements of Chemical Potentials in Pb-Pb Collisions at  $\sqrt{s_{NN}} = 2.76$  TeV". In: *Physical Review Letters* 133.9 (Aug. 2024). ISSN: 1079-7114. DOI: 10.1103/physrevlett.133.092301. URL: <http://dx.doi.org/10.1103/PhysRevLett.133.092301>.
- [5] A Andronic et al. "Hadron yields, the chemical freeze-out and the QCD phase diagram". In: *Journal of Physics: Conference Series* 779 (Jan. 2017), p. 012012. ISSN: 1742-6596. DOI: 10.1088/1742-6596/779/1/012012. URL: <http://dx.doi.org/10.1088/1742-6596/779/1/012012>.
- [6] A. Andronic, P. Braun-Munzinger, and J. Stachel. "Hadron production in central nucleus–nucleus collisions at chemical freeze-out". In: *Nuclear Physics A* 772.3–4 (June 2006), pp. 167–199. ISSN: 0375-9474. DOI: 10.1016/j.nuclphysa.2006.03.012. URL: <http://dx.doi.org/10.1016/j.nuclphysa.2006.03.012>.
- [7] Anton Andronic et al. "The multiple-charm hierarchy in the statistical hadronization model". In: *Journal of High Energy Physics* 2021 (July 2021). DOI: 10.1007/JHEP07(2021)035.

- [8] Carolina Arata. “Measurement of isolated photon-hadron correlations in Pb–Pb collisions at 5.02 TeV with the ALICE experiment at LHC”. Presented 08 Oct 2024. U. Grenoble Alpes, 2024. URL: <https://cds.cern.ch/record/2922803>.
- [9] F. Becattini. *An introduction to the Statistical Hadronization Model*. 2009. arXiv: 0901.3643 [hep-ph]. URL: <https://arxiv.org/abs/0901.3643>.
- [10] Stella Biderman et al. *Pythia: A Suite for Analyzing Large Language Models Across Training and Scaling*. 2023. arXiv: 2304.01373 [cs.CL]. URL: <https://arxiv.org/abs/2304.01373>.
- [11] J. D. Bjorken. “Highly relativistic nucleus-nucleus collisions: The central rapidity region”. In: *Phys. Rev. D* 27 (1 1983), pp. 140–151. DOI: 10.1103/PhysRevD.27.140. URL: <https://link.aps.org/doi/10.1103/PhysRevD.27.140>.
- [12] Elena Botta. “Particle identification performance at ALICE”. In: *5th Large Hadron Collider Physics Conference*. Sept. 2017. arXiv: 1709.00288 [nucl-ex].
- [13] Nicola Semprini Cesaro. *Fisica Subnucleare*. 2024.
- [14] Tiantian Cheng. “Measurements of charm-strange baryon production with ALICE at the LHC”. Presented 27 May 2024. Hua-Zhong Normal U., 2024. URL: <https://cds.cern.ch/record/2908766>.
- [15] ALICE collaboration. “Alignment of the ALICE Inner Tracking System with cosmic-ray tracks”. In: *Journal of Instrumentation* 5.03 (Mar. 2010), P03003–P03003. ISSN: 1748-0221. DOI: 10.1088/1748-0221/5/03/p03003. URL: <http://dx.doi.org/10.1088/1748-0221/5/03/P03003>.
- [16] H David Politzer. “Asymptotic freedom: An approach to strong interactions”. In: *Physics Reports* 14.4 (1974), pp. 129–180. ISSN: 0370-1573. DOI: [https://doi.org/10.1016/0370-1573\(74\)90014-3](https://doi.org/10.1016/0370-1573(74)90014-3). URL: <https://www.sciencedirect.com/science/article/pii/0370157374900143>.
- [17] G Dellacasa et al. *ALICE time projection chamber: Technical Design Report*. Technical design report. ALICE. Geneva: CERN, 2000. URL: <https://cds.cern.ch/record/451098>.
- [18] Zoltán Fodor. “The QCD Phase Diagram and Equation of State”. In: *ELEMENTARY PARTICLE PHYSICS* (Feb. 2021). URL: <https://www.gauss-centre.eu/results/elementaryparticlephysics/the-qcd-phase-diagram-and-equation-of-state>.

- [19] H. Garcilazo, A. Valcarce, and T. F. Caramés. “Charmed baryon–nucleon interaction”. In: *The European Physical Journal C* 79.7 (July 2019). ISSN: 1434-6052. DOI: 10.1140/epjc/s10052-019-7110-z. URL: <http://dx.doi.org/10.1140/epjc/s10052-019-7110-z>.
- [20] Ulrich W. Heinz. *Concepts of Heavy-Ion Physics*. 2004. arXiv: hep-ph/0407360 [hep-ph]. URL: <https://arxiv.org/abs/hep-ph/0407360>.
- [21] Sarah Herrmann. “Measurements of forward charged-particle multiplicity and multiplicity dependence of forward J/ production in pp collisions with the ALICE experiment at LHC”. Presented 24 Oct 2024. U. Lyon 1, IUT, 2024. URL: <https://cds.cern.ch/record/2920632>.
- [22] Nicolo Jacazio. “Production and nuclear modification factors of pions, kaons and protons in pp and AA collisions at the LHC”. PhD thesis. alma, 2019. URL: <http://amsdottorato.unibo.it/9036/>.
- [23] A. Keränen and F. Becattini. “Chemical factors in canonical statistical models for relativistic heavy ion collisions”. In: *Phys. Rev. C* 65 (4 2002), p. 044901. DOI: 10.1103/PhysRevC.65.044901. URL: <https://link.aps.org/doi/10.1103/PhysRevC.65.044901>.
- [24] Peter F. Kolb and Ulrich Heinz. *Hydrodynamic description of ultrarelativistic heavy-ion collisions*. 2003. arXiv: nucl-th/0305084 [nucl-th]. URL: <https://arxiv.org/abs/nucl-th/0305084>.
- [25] Peter F. Kolb, Josef Sollfrank, and Ulrich Heinz. “Anisotropic transverse flow and the quark-hadron phase transition”. In: *Physical Review C* 62.5 (Oct. 2000). ISSN: 1089-490X. DOI: 10.1103/physrevc.62.054909. URL: <http://dx.doi.org/10.1103/PhysRevC.62.054909>.
- [26] Morris Low. “Shoichi Sakata: His Life, the Sakata Model and His Achievements”. In: *Progress of Theoretical Physics Supplement* 167 (Feb. 2007). DOI: 10.1143/PTPS.167.1.
- [27] Saori Maeda et al. “A model of charmed baryon–nucleon potential and two- and three-body bound states with charmed baryon”. In: *Progress of Theoretical and Experimental Physics* 2016.2 (Feb. 2016), p. 023D02. ISSN: 2050-3911. DOI: 10.1093/ptep/ptv194. URL: <http://dx.doi.org/10.1093/ptep/ptv194>.
- [28] Arthur I. Miller. “Werner Heisenberg and the Beginning of Nuclear Physics”. In: *Physics Today* 38.11 (Nov. 1985), pp. 60–68. ISSN: 0031-9228. DOI: 10.1063/1.880993. eprint: <https://pubs.aip.org/physicstoday/article-pdf/38/11/60/7420012/60\_1\_online.pdf>. URL: <https://doi.org/10.1063/1.880993>.

- [29] Michael L. Miller et al. “Glauber Modeling in High-Energy Nuclear Collisions”. In: *Annual Review of Nuclear and Particle Science* 57.1 (Nov. 2007), pp. 205–243. ISSN: 1545-4134. DOI: 10.1146/annurev.nucl.57.090506.123020. URL: <http://dx.doi.org/10.1146/annurev.nucl.57.090506.123020>.
- [30] Takaya Miyamoto et al. “cN interaction from lattice QCD and its application to c hypernuclei”. In: *Nuclear Physics A* 971 (2018), pp. 113–129. ISSN: 0375-9474. DOI: <https://doi.org/10.1016/j.nuclphysa.2018.01.015>. URL: <https://www.sciencedirect.com/science/article/pii/S0375947418300228>.
- [31] S. Navas et al. “Review of particle physics”. In: *Phys. Rev. D* 110.3 (2024), p. 030001. DOI: 10.1103/PhysRevD.110.030001.
- [32] Alexandre Obertelli and Hiroyuki Sagawa. “Modern Nuclear Physics”. In: *Springer Singapore* (2021). ISSN: 2198-7882. DOI: <https://doi.org/10.1007/978-981-16-2289-2>.
- [33] D. Oliinychenko, P. Huovinen, and H. Petersen. “Cooper-Frye Negative Contributions in a Coarse-Grained Transport Approach”. In: *Journal of Physics: Conference Series* 599 (Dec. 2014). DOI: 10.1088/1742-6596/599/1/012017.
- [34] Sonali Padhan. “Multiplicity and energy dependence of (1520) production in pp collisions at  $s = 5.02$  and 13 TeV with ALICE at the LHC”. Presented 29 Jan 2025. Indian Inst. Tech., Mumbai, 2025. URL: <https://cds.cern.ch/record/2924203>.
- [35] Michael E. Peskin and Daniel V. Schroeder. *An Introduction to quantum field theory*. Reading, USA: Addison-Wesley, 1995. DOI: 10.1201/9780429503559.
- [36] Fernando Quevedo and Andreas Schachner. *Cambridge Lectures on The Standard Model*. 2024. arXiv: 2409.09211 [hep-th]. URL: <https://arxiv.org/abs/2409.09211>.
- [37] David Rohr et al. “ALICE HLT TPC Tracking of Pb-Pb Events on GPUs”. In: *Journal of Physics: Conference Series* (2012). URL: <https://dx.doi.org/10.1088/1742-6596/396/1/012044>.
- [38] Luigi Rolandi, Werner Riegler, and Walter Blum. *Particle Detection with Drift Chambers*. Particle Acceleration and Detection. Springer, 2008. DOI: 10.1007/978-3-540-76684-1.
- [39] Golam Sarwar. “Evolution of Perturbation in a Hydrodynamically Expanding System Formed in Relativistic Heavy Ion Collision”. PhD thesis. Aug. 2018. DOI: 10.13140/RG.2.2.10003.53284.

- [40] Bikash Sinha. “Hawking radiation from strange quark nuggets, relics of the QCD phase transition”. In: *Phys. Rev. D* 101 (10 2020), p. 103007. DOI: 10.1103/PhysRevD.101.103007. URL: <https://link.aps.org/doi/10.1103/PhysRevD.101.103007>.
- [41] P. Skands. “Introduction to QCD”. In: *Searching for New Physics at Small and Large Scales*. WORLD SCIENTIFIC, Sept. 2013. DOI: 10.1142/9789814525220\_0008. URL: [http://dx.doi.org/10.1142/9789814525220\\_0008](http://dx.doi.org/10.1142/9789814525220_0008).
- [42] Jan Smit. “Chiral symmetry”. In: *Introduction to Quantum Fields on a Lattice*. Cambridge Lecture Notes in Physics. Cambridge University Press, 2023, pp. 193–228.
- [43] Raimond Snellings. “Elliptic flow: a brief review”. In: *New Journal of Physics* 13.5 (2011), p. 055008. DOI: 10.1088/1367-2630/13/5/055008. URL: <https://dx.doi.org/10.1088/1367-2630/13/5/055008>.
- [44] J. J. de Swart, P. M. M. Maessen, and TH. A. Rijken. *The One-Boson-Exchange Potential Model Approach*. 1994. arXiv: nucl-th/9405008 [nucl-th]. URL: <https://arxiv.org/abs/nucl-th/9405008>.
- [45] D. Teaney, J. Lauret, and E. V. Shuryak. *A Hydrodynamic Description of Heavy Ion Collisions at the SPS and RHIC*. 2001. arXiv: nucl-th/0110037 [nucl-th]. URL: <https://arxiv.org/abs/nucl-th/0110037>.
- [46] *Technical Design Report for the Muon Forward Tracker*. Tech. rep. 2015. URL: <https://cds.cern.ch/record/1981898>.
- [47] A Valcarce et al. “Quark-model study of few-baryon systems”. In: *Reports on Progress in Physics* 68.5 (Mar. 2005), pp. 965–1041. ISSN: 1361-6633. DOI: 10.1088/0034-4885/68/5/r01. URL: <http://dx.doi.org/10.1088/0034-4885/68/5/R01>.
- [48] C. Van Der Leun and C. Alderliesten. “The deuteron binding energy”. In: *Nuclear Physics A* 380.2 (1982), pp. 261–269. ISSN: 0375-9474. DOI: [https://doi.org/10.1016/0375-9474\(82\)90105-1](https://doi.org/10.1016/0375-9474(82)90105-1). URL: <https://www.sciencedirect.com/science/article/pii/0375947482901051>.
- [49] Volodymyr Vovchenko and Horst Stoecker. “Thermal-FIST: A package for heavy-ion collisions and hadronic equation of state”. In: *Computer Physics Communications* 244 (Nov. 2019), pp. 295–310. ISSN: 0010-4655. DOI: 10.1016/j.cpc.2019.06.024. URL: <http://dx.doi.org/10.1016/j.cpc.2019.06.024>.
- [50] Cern webpage. *ALICE*. URL: <https://home.cern/science/experiments/alice>.
- [51] Cern webpage. *ALICE*. URL: [https://alice-collaboration.web.cern.ch/menu\\_proj\\_items/Muon-Spect](https://alice-collaboration.web.cern.ch/menu_proj_items/Muon-Spect).

- [52] Hideki YUKAWA. “On the Interaction of Elementary Particles. I”. In: *Proceedings of the Physico-Mathematical Society of Japan. 3rd Series* 17 (1935), pp. 48–57. DOI: [10.11429/ppmsj1919.17.0\\_48](https://doi.org/10.11429/ppmsj1919.17.0_48).